

**1 Physical and biological processes driving seasonal variability of Nitrate  
2 budget and biological productivity in the Gabon-Congo upwelling system**

**3 Landry Junior Mbang Essome<sup>1,2</sup>, Gaël Alory<sup>1</sup>, Casimir Yelognissé  
4 Da-Allada<sup>2,3,5</sup>, Isabelle Dadou<sup>1</sup>, Roy Dorgeless Ngakala<sup>3,4</sup>, Guillaume  
5 Morvan<sup>1</sup>**

**6** <sup>1</sup>Université de Toulouse, LEGOS (CNES/CNRS/IRD/UT), Toulouse, France

**7** <sup>2</sup>Laboratoire de Géosciences, de l'Environnement et Applications, Université Nationale des  
**8** Sciences Technologies, Ingénierie et Mathématiques, Abomey, Benin.

**9** <sup>3</sup> Department of Oceanography and Applications, International Chair in Mathematical Physics  
**10** and Applications, University of Abomey-Calavi, Cotonou, Benin.

**11** <sup>4</sup> Department of Oceanography and Environment, Institut National de Recherche en Sciences  
**12** Exactes et Naturelles, Pointe-Noire, Congo.

**13** <sup>5</sup>Laboratoire d'Hydrologie Marine et Côtière, Institut de Recherches Halieutiques et  
**14** Océanologiques du Bénin, Cotonou, Bénin.

**15** **Corresponding author** : L.J. Mbang Essome ([landrymbangessome@gmail.com](mailto:landrymbangessome@gmail.com))

**16**

**17**

**18**

**19**

**20**

**21**

**22**

**23**

**24**

**25**

**26**

**27**

**28**

**29**

**30**

**31**

**32**

- 33 Acronyms:
- 34 CTW: Coastally trapped waves
- 35 CoUS: Gabon-Congo Upwelling System
- 36 EKW: Equatorial Kelvin Waves
- 37 GG: Gulf of Guinea
- 38 MLD: Mixed Layer Depth
- 39 SST: Sea Surface Temperature
- 40 SSH: Sea Surface Height
- 41 SLA: Sea Level Anomaly
- 42 CHLa: Chlorophyll-a
- 43 EBUS: Eastern Boundary Upwelling System
- 44 TAUS: Tropical Angolan Upwelling System

45

46

47

48

49

50

51

52

53

54

55

56

57

58

59

60

61

62

63

64

65

66

## 67 Abstract

68 The Gabon-Congo upwelling system, located in the southeastern Gulf of Guinea, is a highly  
69 productive marine ecosystem influenced by both local and remote physical forcing. This study  
70 investigates the seasonal variability of the nitrate budget and biological productivity in this region  
71 using a high-resolution (1/36°) coupled physical-biogeochemical simulation with the NEMO-PISCES  
72 model. The analysis highlights the relative contributions of physical and biological processes in  
73 modulating nitrate concentrations in both the mixed layer and the euphotic zone. Results reveal a  
74 semi-annual cycle of nitrate, with two upwelling periods (May–August and December) and two  
75 downwelling periods (January–April and October–November). These cycles are primarily driven by  
76 the passage of coastal trapped waves (CTWs) forced by equatorial Kelvin waves, inducing vertical  
77 thermocline displacements and regulating nitrate availability in the euphotic zone.

78 The nitrate budget analysis shows that the vertical diffusion linked to internal tide and local wind , and  
79 vertical advection linked to the CTWs, are the dominant process supplying nitrate to the mixed layer  
80 during the main upwelling season. However, near the Congo River mouth (5.5°S–6°S), the horizontal  
81 advection plays a key role, supplying significant amounts of nitrate through the river plume. In the  
82 lower euphotic layer, the vertical mixing contributes to the nitrate loss during the upwelling but  
83 becomes a source of nitrate during the downwelling periods. The seasonal cycle of the chlorophyll-a  
84 (CHLa) concentration follows that of nitrate, confirming that the primary production in this region is  
85 mainly driven by nitrate availability. The study also highlights the role of the Angola Current in  
86 transporting low-nitrate waters from the Equatorial Undercurrent, which influences the nitrate and  
87 CHLa balance in the Gabon-Congo upwelling system.

88 These findings provide new insights into the mechanisms governing nutrient dynamics and biological  
89 productivity in the Gabon-Congo upwelling system. Understanding these processes is crucial for  
90 assessing the impact of climate variability on the regional marine ecosystems and fisheries.

91 **Keywords:** Nitrate Budget, Gabon-Congo Upwelling System, NEMO-PISCES Model,  
92 Physical-Biogeochemical Interactions, Seasonal Variability, Coastal Trapped Waves

93

94

95

96

97

98

99

100

## 101 **1 Introduction**

102 The Eastern Boundary Upwelling Systems (EBUS) are the most productive areas in the global ocean  
103 in terms of biological resources, hosting almost 20% of the world's fisheries (Chavez and Messie,  
104 2009, 2015), even though they only represent around 1% of the world's ocean surface (Freon et al.,  
105 2009). They are therefore an important economic support for the countries bordering these areas (Carr  
106 et al., 2002). EBUS are controlled by wind stress blowing parallel to the coast, generating an offshore  
107 Ekman transport leading to coastal upwelling of cold and nutrient-rich waters, which trigger primary  
108 production in the euphotic layer, with increased surface chlorophyll-a (CHLa) concentration visible on  
109 satellite images (e.g. Gutknecht et al., 2013). Besides their ecological richness, EBUS act as active  
110 interfaces for greenhouse gases. They are recognized as significant sources of  $N_2O$ , primarily due to  
111 the oxygen minimum zone (OMZ) that favors subsurface production (Gutknecht et al., 2013;  
112 Resplandy et al., 2024). Regarding  $CO_2$ , while cold surface waters enhance gas solubility, the vigorous  
113 upwelling of deep waters rich in Dissolved Inorganic Carbon (DIC) generally dominates this thermal  
114 effect, driving net  $CO_2$  outgassing near the coast (Resplandy et al., 2024).

115 Beyond these EBUS, recent studies (Bachèlery et al., 2016; Kopte et al., 2017; Awo et al., 2022) have  
116 shown that the variability of Sea Surface Temperature (SST, a key upwelling indicator) at the eastern  
117 boundary of the South Atlantic was not only impacted by local wind forcing, but also by remote  
118 forcing initiated by the equatorial dynamics. Indeed, the equatorial Kelvin waves (EKW) propagating  
119 along the equator and later poleward along the coast as coastal trapped waves (CTW) have been shown  
120 to lead to the establishment of seasonal upwelling systems.

121 This is the case for the Gabon-Congo and Angolan tropical upwelling systems, located in the  
122 south-east of the Gulf of Guinea (GG), which are highly productive marine ecosystems (Ostrowski et  
123 al., 2009). Fishing provides around 25% of the Angolan population's total animal protein intake and is  
124 essential for economic security (Hutchings et al., 2009; Sowman and Cardoso, 2010; FAO, 2022). The  
125 seasonal variability of SST along the Angolan coast has shown an evolution that was similar to that  
126 observed in the Congo (Bachèlery et al., 2015, 2016; Kopte et al., 2017; Awo et al., 2022; Brandt et al.,  
127 2023). It is characterized by a semi-annual pattern with an initial warming in February-April followed  
128 by a first upwelling-induced cooling in May-August. Then there is a second warming, less significant  
129 than the first, in September-November, followed by a second, less significant cooling in  
130 December-January. Following to Radenac et al. (2020) and Brandt et al. (2023), in the tropical Atlantic  
131 ocean, the thermocline and nitracline were often found at the same depth, which meant that an upward  
132 movement of the thermocline was associated with upward advection of nitrate, fueling biological  
133 productivity. Brandt et al. (2023) also pointed out that in the Angolan tropical upwelling system, the  
134 seasonal cycle of nitrate was in phase with that of CHLa derived from ocean color satellites (Fig. 1).  
135 Given that the wind stress along the coast was low for most of the year and out of phase with the

136 upwelling period, the upwelling was rather shown to be induced by the passage of waves trapped at the  
137 coast, which signature was visible on the seasonal cycle of the sea level anomaly (Bachèlery et al.,  
138 2016; Awo et al., 2022; Brandt et al., 2023).

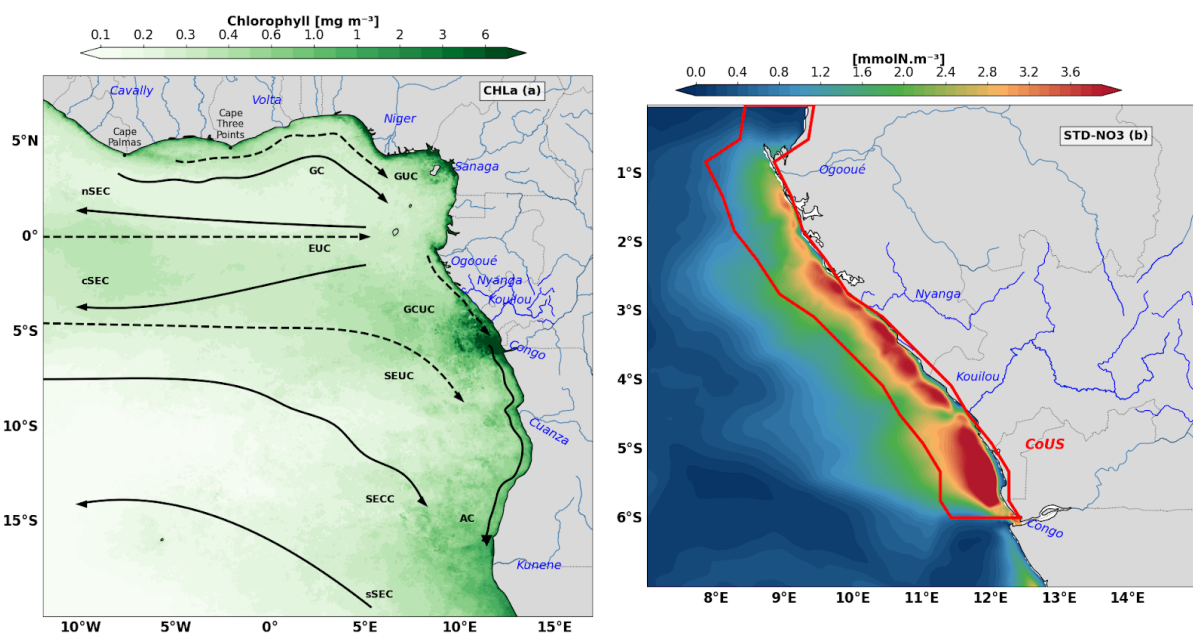
139 The cross-shore extension of the zone covered by upwelling is modulated by the regional ocean  
140 circulation (Fig. 1), dominated by the southward coastal Angola Current and Congo-Gabonese  
141 Undercurrent (Kopte et al., 2017; Bachèlery et al., 2016; Awo et al., 2022). Bachèlery et al. (2016),  
142 based on a coupled physical-biogeochemical model, showed that equatorial remote forcing is dominant  
143 for the interannual variability of nutrients and primary production, whereas the local wind stress  
144 forcing is dominant for the sub-seasonal variability. Some studies also highlighted the important role  
145 played by turbulent mixing, locally enhanced in shallow waters near the coast (Körner et al., 2023,  
146 2024; Tchipalanga et al., 2018a; Rouault, 2012), in the seasonal modulation of SST and nutrients in  
147 Angolan coastal waters.

148 The Gabon-Congo upwelling zone (from 0°N to 6°S) is poorly documented. In a recent study using a  
149 high resolution (1/36°) simulation of the NEMO model over the GG, Ngakala et al. (2025) assessed  
150 the seasonal mixed layer heat budget in the Congolese upwelling system. They found that the mixed  
151 layer heat budget in the Congolese coastal area was driven by two major processes: warming by heat  
152 fluxes, dominated all year long by the solar flux, and cooling by vertical mixing at the base of the  
153 mixed layer. whereas the total advection contribution is less important, it plays a secondary role in the  
154 mixed layer heat budget. However, below the mixed layer, vertical advection by upwelling CTWs was  
155 crucial to raise the thermocline high enough so that cool waters can penetrate in the mixed layer by  
156 vertical mixing. They also mentioned that the relative contribution of vertical advection and diffusion  
157 in the mixed layer heat budget was sensitive to the criterion used to define the mixed layer.

158 These results were in agreement with the conclusion of Körner (2023) in the northern Angolan  
159 upwelling south of the Congo River mouth. This latter study found that the net surface heat flux  
160 warmed the coastal water further, whereas turbulent mixing across the base of the mixed layer was an  
161 important cooling term. Also, Scannell and McPhaden (2018), using data from a PIRATA mooring  
162 located off the Congo River at [8°E; 6°S], found that the seasonal evolution of mixed layer properties  
163 had two main phases: a warm fresh phase (December-April) when solar heating was very efficient in  
164 warming SST in a thin mixed layer, and a cold-salty phase (May-September) driven by the  
165 intensification of southeasterly trades in response to the onset of the West African Monsoon and  
166 northward displacement of the ITCZ. They also pointed out the necessity to take into account  
167 precipitation influence in the mixed layer heat budget.

168 Little information has been available at the seasonal scale for biogeochemistry in the GG. In the  
169 equatorial upwelling system, the respective contributions of physical and biological processes on the

170 seasonality of nitrate and biological productivity, in the mixed layer and euphotic layer, have been  
 171 quantified by Radenac et al. (2020). Along the coast, most studies of biogeochemical dynamics have  
 172 been either limited to the section between 6°S and the Angola Benguela frontal zone (Brandt et al.,  
 173 2023), or have focused on the interannual variability of biogeochemical tracers (Bachelery et al.,  
 174 2016). The seasonal variability of biogeochemical tracers and biological productivity between 0°N and  
 175 6°S is likely influenced by three major processes: coastal upwelling, input of nutrients by the Congo  
 176 River discharge (which is the second largest river discharge in the world; Hopkins et al., 2013), and the  
 177 stratification linked to the Congo River freshwater. The aim of this paper is to investigate the  
 178 respective roles of physical and biological processes in the seasonal cycle of nitrate and CHLa  
 179 concentration, and the respective contributions of coastal upwelling and Congo River discharge to the  
 180 biological productivity in the Gabon-Congo upwelling system. The paper is organized as follows:  
 181 Section 2 describes the numerical model and datasets; Section 3 presents the model validation and the  
 182 nitrate budget analysis; Section 4 discusses the physical-biological interactions, and Section 5 provides  
 183 the conclusions.



184

185 **Figure 1:** Regional ocean circulation and spatial distribution of biological and nutrient tracers.

186 (a) Annual mean surface Chlorophyll-a concentration ( CHLa,  $\text{mg m}^{-3}$ ). The map illustrates the spatial  
 187 distribution of biological productivity across the Gulf of Guinea and the South Atlantic African margin. Black  
 188 arrows and dashed lines indicate the major surface and subsurface currents: northern, central and southern  
 189 branches of the South Equatorial Current (nSEC, cSEC and sSEC , respectively), Equatorial Undercurrent  
 190 (EUC), Guinea Current (GC), Guinea Undercurrent (GUC), Gabon-Congo Undercurrent (GCUC), South  
 191 Equatorial Undercurrent (SEUC), South Equatorial Counter Current (SECC), and Angola Current (AC). (b)  
 192 Standard deviation of Nitrate concentration ( STD-NO3,  $\text{mmolN m}^{-3}$ ). The color scale represents the  
 193 variability of nitrates in the upper ocean. The red polygon delimits the coastal domain defined as the  
 194 Gabon-Congo Upwelling System (CoUS), extending from the Congo River mouth ( $\sim 6^\circ\text{S}$ ) to the Equator ( $\sim 0^\circ\text{S}$ ),

195 which serves as the primary study area for the nutrient budget analysis. Blue labels highlight the discharge points  
196 of the Ogooué, Nyanga, Kouilou, and Congo rivers.

## 197 **2 Data and methods**

### 198 **2.1 Numerical model**

199 To understand the dynamics in the Gabon-Congo upwelling system, we have used the NEMO  
200 (Nucleus for European Modelling of the Ocean) ocean general circulation model based on the  
201 primitive equations discretized on an Arakawa-C grid (Madec et al., 2024). The vertical mixing is  
202 computed from a turbulent closure scheme using the GLS (Generic Length Scale) formulation.

203 In this work, the NEMO model was coupled with PISCES (Pelagic Interactions Scheme for  
204 Carbon and Ecosystem Studies), a biogeochemical model developed by Aumont et al. (1998) and  
205 subsequently improved. Here, the version used is PISCES-2 (Aumont et al., 2015). This model has  
206 three main compartments: the first represents nutrients, including nitrogen compounds (nitrate and  
207 ammonium), iron, phosphate and silicates; the second represents phytoplankton and includes two  
208 classes, nano-phytoplankton and diatoms; the third compartment represents zooplankton, made up of  
209 two classes, microzooplankton and meso-zooplankton. We used the PISCES (cell quotas) model with  
210 constant Redfield ratios (Aumont and Bopp, 2006; Aumont et al., 2015).

211 A regional configuration of the GG (11°S - 6°N; 10°W - 14°E) with an horizontal resolution  
212 of 1/36° and 50 vertical levels is used. The atmospheric forcing is derived from the JRA-55 reanalysis  
213 of the Japanese meteorological agency (Kobayashi et al. 2015), except for the wind forcing which is  
214 based on daily ASCAT (Advanced SCATterometer) satellite data at 1/4° spatial resolution. Lateral  
215 boundaries conditions are from Mercator GLORYS12V1 reanalysis data at 1/12° spatial resolution for  
216 physics and NEMO-PISCES reanalysis at 1/4° of Radenac et al. (2020) for biogeochemistry.  
217 Continental freshwater inputs for this configuration are derived from the ISBA-CTRIP model, and in  
218 situ data from the HYBAM network for the Congo River. The NEMO configuration, ran over the  
219 period 2007-2017 (after a two-year spin-up), was validated by Ngakala et al. (2025) in our region of  
220 study. This simulation has also been validated and used in the Northern Gulf of Guinea for the coastal  
221 upwelling in summer and its interaction with mesoscale dynamics (Thiam et al., 2024). The reference  
222 simulation of the coupled biogeochemical physical model (NEMO-PISCES) was produced over the  
223 period 2007-2011, with a spin-up of 4 years for the biogeochemical part (2007-2010). We analysed  
224 monthly and daily outputs for the year 2011, which is characterised by neutral conditions regarding the  
225 Atlantic Niño and Benguela Niño interannual variability (Brandt et al., 2023).

226 .

227

## 228 2.2 Satellite and in-situ data

229 Several observational products were used to assess the model's ability to reproduce the physical and  
230 biogeochemical characteristics of the area for the year 2011. We used the MUR product (Multi-scale  
231 Ultra-high Resolution; Chin et al., 2017) with  $1/4^\circ$  spatial resolution and daily temporal resolution to  
232 assess the regional distribution and the seasonal cycle of SST. The vertical temperature distribution  
233 was assessed using the World Ocean Atlas (WOA; Locarnini et al., 2018; Zweng et al., 2019)  
234 climatology. The CHLa data used came from the Globcolour product distributed by Copernicus Marine  
235 Environment Monitoring Service (<http://marine.copernicus.eu/>), which combines data from four ocean  
236 color satellites, with very high spatial resolution (1 km) and daily temporal resolution.

237 The nutrient fields were assessed using the CSIRO Atlas of Regional Seas climatology  
238 (Ridgway and Dunn, 2002) which merges several in situ databases (Argo buoys, WOD2005, WOCE3,  
239 Global Hydrographic Program, CTD and CMAR4 hydrology archives, NIWA5 hydrographic data, and  
240 CRC6 hydrographic data). It provides physical variables (Temperature, Salinity) and biogeochemical  
241 variables ( $NO_3$ ,  $PO_4$ ,  $O_2$ , Si) both at the surface and at depth with a horizontal resolution of  $1/2^\circ$ , 79  
242 vertical levels from the surface to 5500 m depth, with a step of 5 m near the surface then increasing  
243 with depth, and a daily temporal resolution. This product was built from 2009 and contains data from  
244 1940 until 2011 which was the date when the last revision of the product was made. Near surface  
245 currents from the Ocean Surface Current Analysis Real-time (OSCAR, Johnson et al. 2007) dataset are  
246 based on satellite and in situ measurements of sea surface height surface vector wind and SST. They  
247 are derived from quasi-linear and steady flow momentum equations thus combine geostrophic, Ekman  
248 and Stommel shear dynamics. OSCAR product is available on a  $1/3^\circ \times 1/3^\circ$  grid with a 5-day temporal  
249 resolution for year 2011, and we use it to validate the near surface currents (first 30 meters) of the  
250 model outputs. Sea Level Anomaly was computed from the salto/duacs gridded product of Absolute  
251 Dynamic Topography for 2011. This product is based on sea surface height measurement of  
252 multission altimeters since 1992, optimally interpolated onto  $0.25^\circ \times 0.25^\circ$  longitude/latitude grid  
253 (Ducet et al., 2000).

## 254 2.3 Methods

255 The variability of nutrients and in particular nitrate is driven by several physical and biogeochemical  
256 processes taken into account in our model. As in Radenac et al (2020), the nitrate budget integrated  
257 over the mixed layer depth is represented by the following equation:

$$258 \frac{\partial \langle NO_3 \rangle}{\partial t} = - \langle u \frac{\partial NO_3}{\partial x} \rangle - \langle v \frac{\partial NO_3}{\partial y} \rangle - \langle w \frac{\partial NO_3}{\partial z} \rangle + \frac{1}{h} \left( K_z \frac{\partial NO_3}{\partial z} \right)_{z=-h} - \frac{1}{h} \frac{\partial h}{\partial t} \left( \langle NO_3 \rangle - NO_{3_{z=-h}} \right)$$

259  $+ SMS(NO_3)$  (1)

260 In Equation (1), the term on the left represents the total nitrate tendency, where the brackets  $\langle \dots \rangle$   
 261 denote the vertical average within the mixed layer of depth  $h$ . This depth  $h$  is defined as the level  
 262 where the potential density exceeds the reference density at 3 meters by approximately  $0.06 \text{ kg/m}^3$   
 263 (Aroucha et al., 2025). On the right side of the equation, the first three terms represent the zonal,  
 264 meridional, and vertical advectons of nitrate, respectively, with  $u, v$  and  $w$  being the components of the  
 265 velocity field. The fourth term represents the vertical diffusion (mixing) at the base of the mixed layer  
 266 ( $z=-h$ ), where  $K_z$  is the vertical diffusion coefficient that varies in space and time. The fifth term  
 267 corresponds to the entrainment term, which represents the flux of nitrate into the mixed layer during its  
 268 deepening. However, it is not explicitly solved in our budget analysis. Following Radenac et al. (2020)  
 269 for the tropical Atlantic using a similar NEMO-PISCES configuration, this term is negligible  
 270 compared to other terms in the budget. Finally, the SMS (Source Minus Sink) term represents the  
 271 contribution of biological processes to the spatial and temporal variability of  $\text{NO}_3$  concentrations, as  
 272 detailed in the following expression:

$$273 \text{SMS}(\text{NO}_3) = \text{Nitri}f - \mu_{\text{NO}_3}^P * P - \mu_{\text{NO}_3}^D * D - R_{\text{NH}_4} * \lambda_{\text{NH}_4} * \Delta(\text{O}_2) * \text{NH}_4 - R_{\text{NO}_3} * \text{Denit} \quad (2)$$

274 where *Nitri*f corresponds to nitrification, which is the conversion of ammonium into nitrate by  
 275 bacterial activity. It is parameterized by:

$$276 \text{Nitri}f = \lambda_{\text{NH}_4} - \frac{\text{NH}_4}{1 + \langle \text{PAR} \rangle} (1 - \Delta(\text{O}_2)) \quad (3)$$

277 where  $\text{NH}_4$  is the ammonium concentration,  $\langle \text{PAR} \rangle$  is the average fraction of solar radiation available  
 278 for photosynthesis,  $\lambda_{\text{NH}_4}$  is the nitrification rate and  $\Delta(\text{O}_2)$  is the oxygen variation in the mixed layer,  
 279 which provides information on the oxic and anoxic conditions of the water column: The second and  
 280 third terms on the right of equation (2) are the growth of nanophytoplankton and diatoms, where  $\mu_{\text{NO}_3}^P$   
 281 and  $\mu_{\text{NO}_3}^D$  are their growth rates,  $P$  and  $D$  are their concentrations respectively.  $R_{\text{NH}_4}$  and  $R_{\text{NO}_3}$  are the  
 282 stoichiometric  $N/C$  ratios of ammonification and nitrification respectively.. *Denit* represents  
 283 denitrification which occurs when the water becomes anoxic, and so nitrate (instead of oxygen) is  
 284 consumed by remineralization of organic matter. A detailed description of the terms of these equations  
 285 is given by Aumont et al (2015). We used the parameter PISCES values modified for the Tropical  
 286 Atlantic ocean from Radenac et al. (2020). The balance terms in equation (1) have been calculated  
 287 online for 2011. As the lateral diffusion term is generally negligible compared with the others, it will  
 288 not be discussed further.

289 Since the advection in (1) depends on both nitrate gradients and velocities, we investigate which  
 290 component primarily controls its contribution. First, we analyze the seasonal evolution of gradient and

291 velocity following Awo et al. (2022). Second, we evaluate the individual contributions of seasonal  
 292 variations in velocity and gradient, as well as their combined effect, following Topé et al. (2023),  
 293 according to equation (4).

$$294 \left( V_i \cdot \nabla_i (NO_3) \right)' = V_i' \cdot \overline{\nabla_i (NO_3)} + \overline{V_i} \cdot \nabla_i (NO_3)' + V_i' \cdot \nabla_i (NO_3)' \quad (4)$$

295 The total seasonal variation of the advection term is thus decomposed into three distinct contributions:

296  $V_i' \cdot \overline{\nabla_i (NO_3)}$  (Current variability), this term quantifies the impact of current velocity anomalies acting  
 297 upon a mean (steady-state) nitrate distribution. It isolates the effect of current acceleration or  
 298 intensification (such as the SEUC or the Angola Current) on nutrient transport.  $\overline{V_i} \cdot \nabla_i (NO_3)'$  (Gradient  
 299 variability), this term represents the impact of seasonal changes in the nitrate concentration gradient  
 300 under a mean circulation. It highlights the influence of seasonal water mass enrichment, particularly  
 301 via the Congo River plume.  $V_i' \cdot \nabla_i (NO_3)'$  (Non-linear term), this term accounts for the simultaneous  
 302 interaction between current fluctuations and gradient fluctuations. To determine which of these  
 303 mechanisms predominantly governs the nitrate budget, Pearson correlation coefficients were  
 304 calculated between the total advective anomaly and each decomposed component. This statistical  
 305 approach serves a critical physical objective: it allows us to disentangle whether the seasonal nitrate  
 306 supply is driven primarily by the kinematic modulation of the flow (circulation-driven) or by the  
 307 pulsing of the nutrient source (supply-driven). A high correlation with the current term would identify  
 308 regional circulation such as the SEUC or Angola Current as the primary pump, whereas a dominant  
 309 correlation with the gradient term would pinpoint the massive periodic enrichment, particularly from  
 310 the Congo River plume, as the main trigger of nitrate variability. All reported correlations are  
 311 statistically significant at a 95% confidence level ( $p < 0.05$ ). By establishing this statistical hierarchy,  
 312 we can physically characterize the system as being either transport-limited or supply-limited,  
 313 providing a rigorous diagnostic of the processes regulating primary productivity in the Gabon-Congo  
 314 upwelling. The Primary production (NPP) was calculated from the phytoplankton evolution equation  
 315 (Aumont et al 2015):

$$316 \quad NPP = (1 - \delta^P) \mu^P * P \quad (5)$$

317 In this equation, P is the phytoplankton biomass (diatoms),  $\delta^P$  represents the exudation of the  
 318 phytoplankton (diatoms).  $\mu^P$  is the specific growth rate of the phytoplankton taking into account  
 319 nutrient and light availability. Note that this equation applies to each phytoplankton species (diatoms  
 320 or nanophytoplankton), and total NPP is the sum of NPP from both diatoms and nanophytoplankton.  
 321  $\mu^P$  is the specific growth rate of the phytoplankton taking into account nutrient and light availability.

322 NPP, which represents the organic matter synthesized by phytoplankton after accounting for  
323 autotrophic respiration, is calculated online by the coupled NEMO-PISCES model. Within the model  
324 framework, NPP is partitioned into New Production (NP), fueled by external nutrient inputs (primarily  
325 nitrate) through advection and diffusion, and Regenerated Production (RP), sustained by nutrients  
326 recycled within the euphotic zone (primarily ammonium). Both NP and RP components are computed  
327 online, providing a detailed breakdown of the trophic status and nutrient utilization efficiency in the  
328 Gabon-Congo upwelling system.

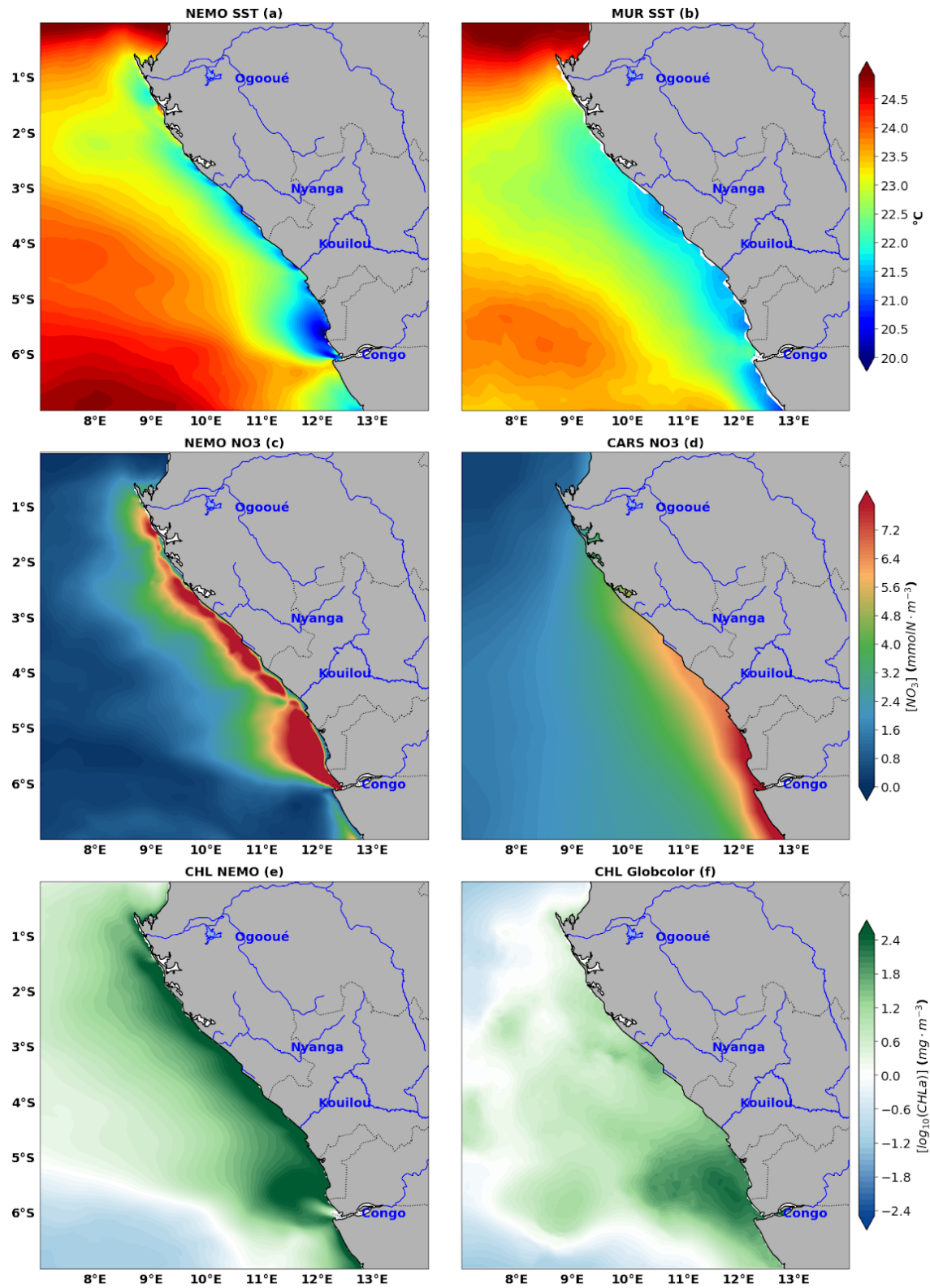
329

## 330 **3 RESULTS**

### 331 **3.1 Model/data comparison**

#### 332 **3.1.1 Spatial variations during the upwelling period**

333 The assessment of our model simulation has been done using several observation products of physical  
334 variables , including Sea Surface Temperature (SST), Sea Surface Height (SSH), and ocean currents,  
335 as well as biogeochemical tracers such as nitrate ( $\text{NO}_3$ ) and CHLa, based on both satellite and in situ  
336 data. Fig.2 shows the regional distribution from observations and model outputs for both SST  
337 (Fig.2a-b), nitrate concentration (Fig.2c-d) and CHLa concentration (Fig.2e-f), averaged for austral  
338 winter (June,July and August) which is the main Gabon-Congo upwelling period (Ngakala et al.,  
339 2025). As can be seen, the upwelling feature is well captured by the model with cooling of surface  
340 water at the coast below  $23^\circ\text{C}$  in the model and  $22^\circ\text{C}$  in the MUR product (Fig. 2a,b). This cooling  
341 feature is consistent with high nitrate (Fig. 2c,d) and CHLa (Fig. 2e,f) concentrations in both models  
342 and observation, particularly north of the Congo estuary ( $6^\circ\text{S}$ ) and nearby Kouilou River mouth (Fig.  
343 2e) at  $4.47^\circ\text{S}$ . These cool and enriched nutrient coastal waters are spread offshore displaying a  
344 cross-shore gradient, with a greater extension in the observation than the model. The highest nitrate  
345 concentration in the coastal waters is greater than  $10 \text{ mmolN.m}^{-3}$  in the model ( $8 \text{ mmolN.m}^{-3}$  in the  
346 observation) located mainly in the Congo River plume area, inducing enhancement of PP resulting in a  
347 strong CHLa signature.



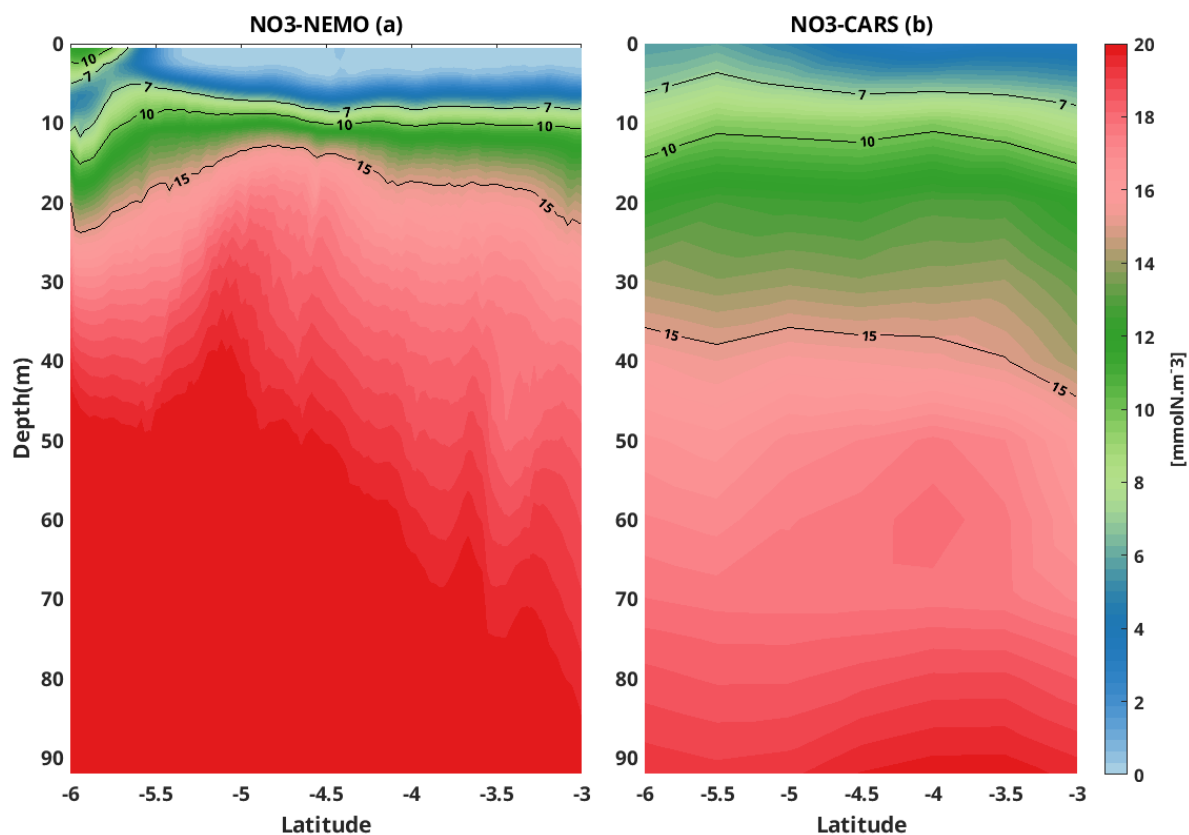
348

349 **Figure 2:** Comparison between model (left hand side) and observations (right hand side) with regional  
 350 distribution of sea surface temperature (a, b), nitrate concentration (c, d) and CHLa concentration (e, f)  
 351 averaged for austral winter (June, July, August)

352 The offshore area (7°E-10°E) is the oligotrophic zone characterized by relatively warm waters (24.5°C  
 353 in the model and 23.5°C in the observation), depleted in nitrate and less productive in CHLa  
 354 concentration. In this offshore area nitrate concentrations are lower than 1.6 mmolN.m<sup>-3</sup> in the  
 355 observation and 0.8 mmolN.m<sup>-3</sup> in the model.

356 Although the model captures relatively well the regional distribution of the 3 variables, we can see  
 357 some differences. For instance, the model is warmer than observations by about 1°C and shows  
 358 stronger nitrate concentration (by about 2 mmolN.m<sup>-3</sup>) and CHLa concentration (6-10 mg.m<sup>-3</sup>) at the  
 359 coast. In the offshore area, the model seems to be less enriched in nitrate concentration than the  
 360 observation by about 0.8 mmolN.m<sup>-3</sup>.

361 High variability of nitrate concentration is found in the coastal Gabon-Congo area (Fig.1b) and in the  
 362 Congo river plume zone as we can see in model annual standard deviation distribution of NO<sub>3</sub>.  
 363 Therefore the red box (0°S-6°S, 1° width coastal band) in Fig.1b is used to analyze the vertical nitrate  
 364 profile to assess the model's ability to capture its vertical distribution. This area corresponds to our  
 365 studied area in the Gabon-Congo coastal upwelling zone.

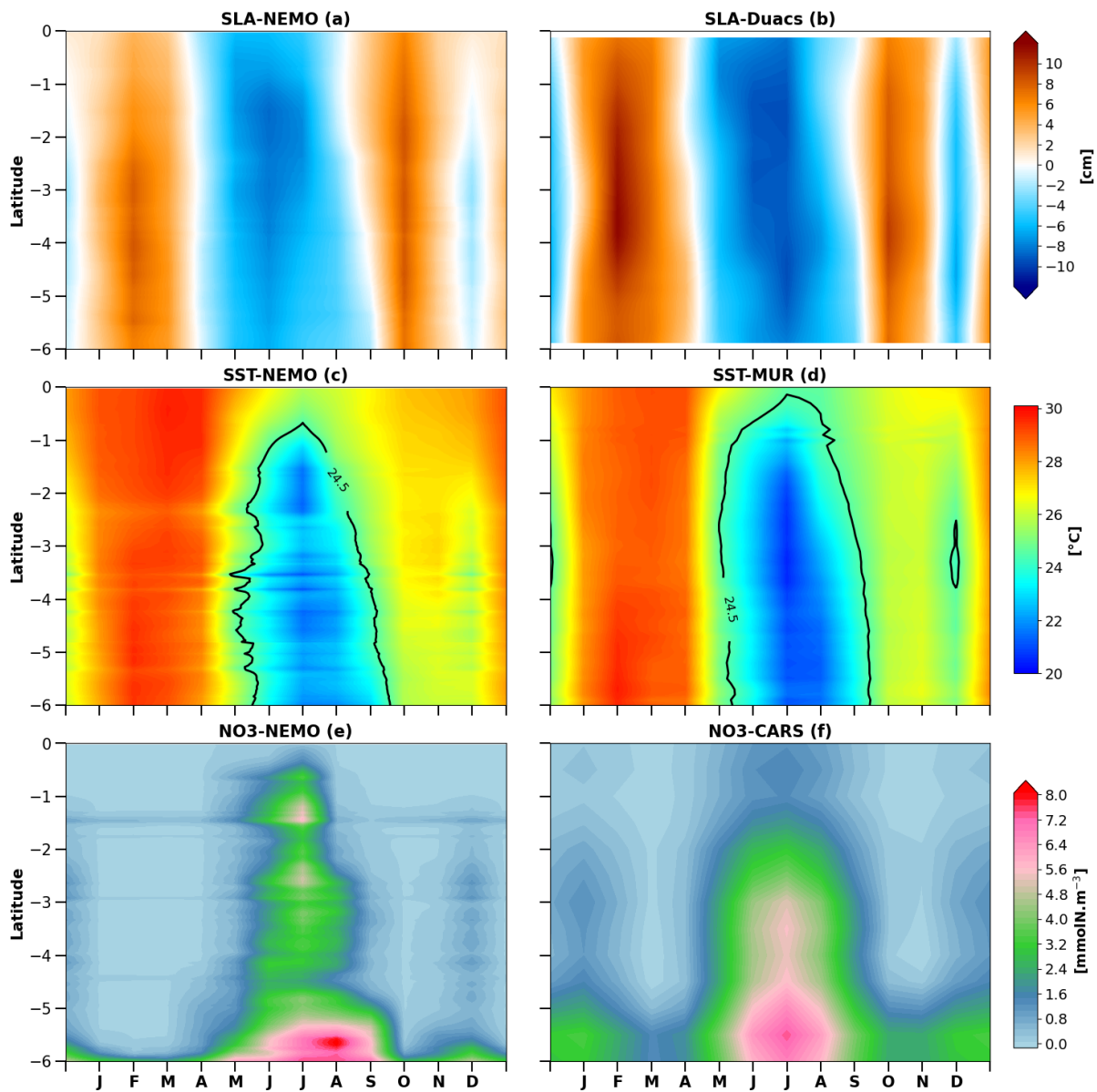


366  
 367 **Figure 3:** Comparison between model (a) and observation (b) using vertical distribution of nitrate concentration  
 368 in the first 90 m, in the coastal box (3°S-6°S and 1° width band to the coast) in the main upwelling season (June,  
 369 July and August). black represents nitrate concentration isolines.

370 Very close to the surface, water masses are nutrient depleted for both model and observation (Fig.3),  
 371 likely due to photosynthesis activity of phytoplankton that consumes nitrate in presence of light,

372 increasing its biomass thus CHLa concentrations. However this depletion is more pronounced in the  
 373 model than in the observation. In the subsurface, the high nitrate concentration is due to the  
 374 remineralization of organic matter by bacteria and coastal upwelling of deeper enriched nitrate waters,  
 375 with the model showing higher concentrations than observed. Although nitrate isolines are shallower  
 376 in the model than in observations below about 15 m depth, some nitrate isolines are relatively well  
 377 captured by the model, for instance isolines 7 and 10  $\text{mmolN.m}^{-3}$ .

### 378 3.1.2 Seasonal cycle of SST, nitrate, SLA and current in the Gabon-Congo coastal area



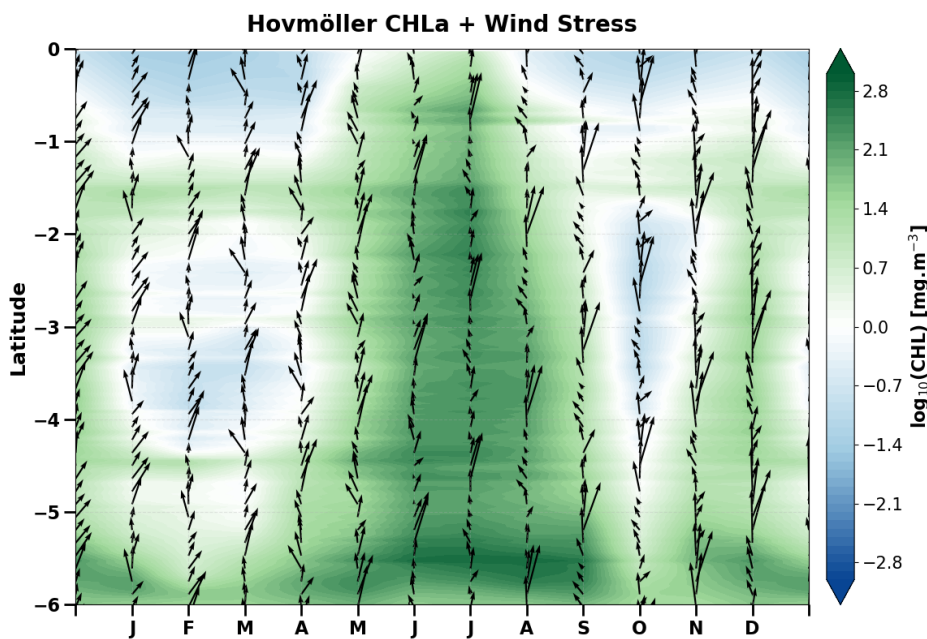
379  
 380 **Figure 4:** Comparison between modeled (left) and observed (right) seasonal cycles of Sea Level Anomaly (a, b),  
 381 SST(c, d) and nitrate concentration (e, f) averaged in the coastal box ( $6^{\circ}\text{S}-0^{\circ}\text{S}$ ,  $1^{\circ}$  width).

382 Now we use the coastal box defined in Fig. 1b to evaluate the seasonal cycle of nitrate. The nitrate  
 383 seasonal variability is characterized by a semi-annual cycle with two maxima and two minima in the

384 model and the observations. The main maximum occurs from May to September when SST reaches its  
385 minimum of 20°C in both model and observations (Fig.4c, Fig.4d) and the secondary maximum occurs  
386 in December when SST reaches a secondary minimum of 25.5°C in the model and 24.5°C in  
387 observation. We have a warmer SST reaching 30°C from January to April and 26°C from October to  
388 November in both the model and the observations. This semi-annual SST cycle is likely due to CTWs  
389 propagation since it is consistent with the SLA seasonal cycle (minimum SST corresponds to negative  
390 SLA and maximum SST corresponds to positive SLA) as mentioned earlier by Ngakala et al. (2025) in  
391 the same area. Indeed, the propagation of CTWs induce vertical migration of the thermocline resulting  
392 thereby in cooling or warming at the surface. At the seasonal scale, the propagation of upwelling  
393 CTWs from May to September and in November-December uplifts thermocline, supplying cold waters  
394 to the surface and reducing Sea Surface Height (SSH) by steric effect. As downwelling CTWs  
395 propagate from January to April and in September-October, they deepen thermocline, warming the  
396 surface and increasing SLA. The cold waters upwelled by CTWs (May-September) are highly  
397 enriched in nitrate, whereas warm surface waters induced by downwelling CTWs (January-April and  
398 September-October) are nitrate depleted. The seasonal variability of SLA due to CTWs (Fig.4a,  
399 Fig.4b) is consistent with the seasonal variability of SST (Fig.4c, Fig.4d) and of nitrate concentration  
400 (Fig.4e, Fig.4f) in both the model and observations. The highest nitrate concentration is around 10  
401  $\text{mmol.m}^{-3}$  near the Congo River mouth (6°S) and decreasing northward, however the observations  
402 seem to be richer in nitrate than the model. In December during the secondary cooling, nitrate  
403 concentration in the model is greater by about 1.2  $\text{mmol.m}^{-3}$  than observed along the coast. In the  
404 warming period (January-April and October-November), this coastal area seems to be nitrate depleted.  
405 Despite the model capturing the SLA signature, the observed seasonal cycle of SLA remains more  
406 intense than in the simulation. This feature is driven by the combined effect of remotely forced  
407 Equatorial Kelvin Waves (EKW) and poleward-propagating CTWs (Bachèlery et al., 2016; Kopte et  
408 al., 2017; Awo et al., 2023; Brandt et al., 2023). During cooling periods, upwelling CTWs decrease the  
409 SLA and uplift the thermocline. Following Radenac et al. (2020), the thermocline depth in this region  
410 acts as a reliable proxy for the nitracline; its upward migration significantly enhances nitrate supply to  
411 the surface, fueling biological productivity. Conversely, the downwelling waves observed in the  
412 warming periods increase the SLA and deepen the nitracline, leading to the nutrient-depleted  
413 conditions described previously.

414 High nitrate concentrations support biological production, therefore correspond to high CHL<sub>a</sub> signals  
415 at the surface (Fig.5). On the contrary, during the warming period, the downwelling CTWs  
416 propagating along the coast increase SLA, deepen the thermocline (Ngakala et al. (2025). This also  
417 deepens the nitracline and consequently deplete the nitrate concentration at the ocean surface, thus the  
418 low CHL<sub>a</sub> signal (Fig.5).

419 The variability of simulated near-surface currents between 0 to 15 m depth (Fig.6) was compared to  
 420 the OSCAR product. Here, we make a latitudinal section at 4°S and look at the seasonal cycle of  
 421 meridional currents (Fig.6a and 6b) from 7°E to the coast for both the model (Fig.6a) and observations  
 422 (Fig.6b). We do not restrict to the Gabon-Congo box as we have done for other variables, because the  
 423 OSCAR product is not well resolved at the vicinity of the coast. So we can see that the model  
 424 reasonably represents the seasonal variability of meridional currents with northward velocities in  
 425 April, June-September and November-December with the magnitude of around 0.1 m.s<sup>-1</sup>. In the  
 426 observations, this structure is more or less similar, but we can see some differences: southward  
 427 velocities between 8.5°E and 10.2°E in July, and also between 7°E and 9°E during August-September  
 428 and January, are not found in the model.



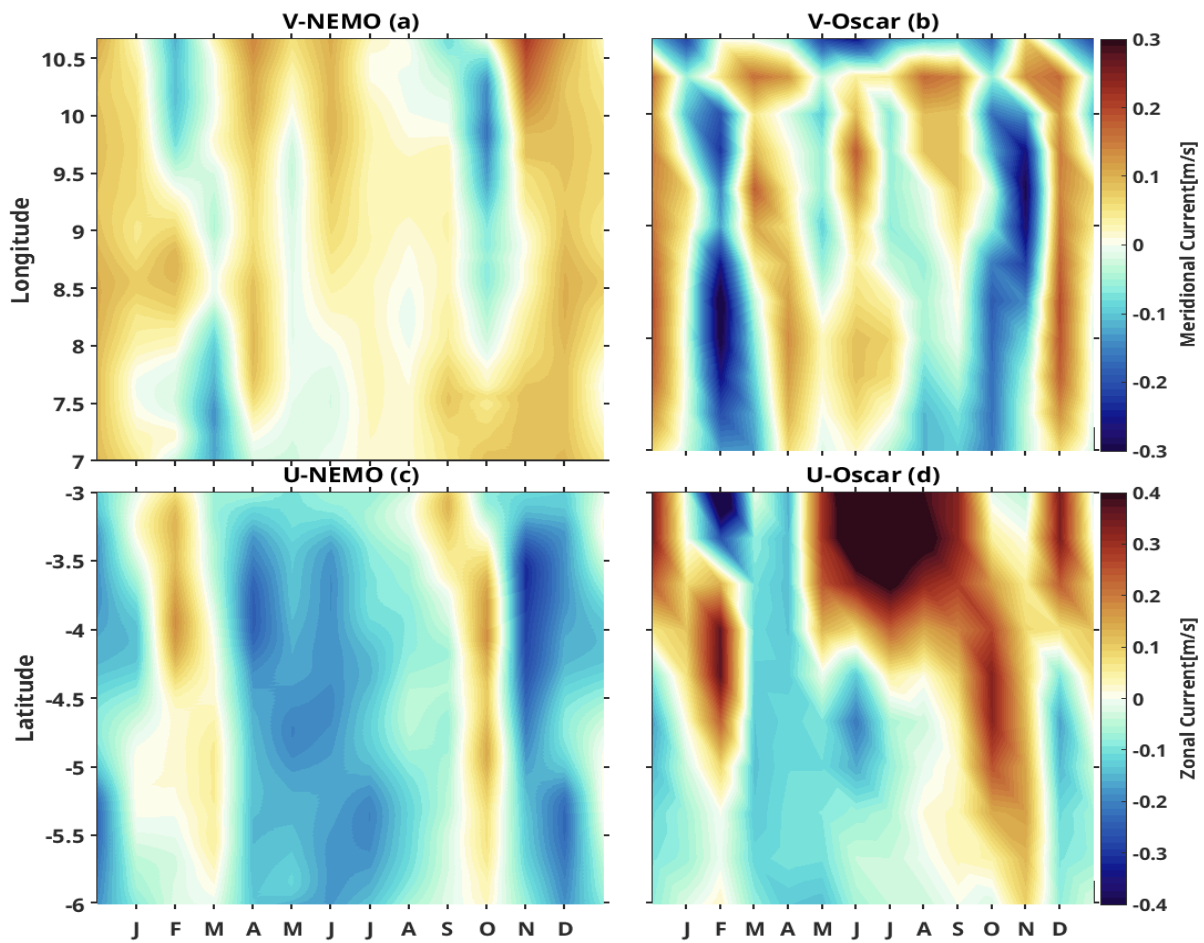
429  
 430 **Figure 5:** Seasonal cycle of CHLa concentration (in background) and wind stress (black arrow) along the  
 431 Gabon-Congo coastal box (6°S-0°S, 1° width) area in the model.

432 Nevertheless, we can see in both products southward currents in February-March and October with a  
 433 strong magnitude of 0.25 m.s<sup>-1</sup> in the observations though only 0.15 m.s<sup>-1</sup> in the model. This seasonal  
 434 structure is consistent with the seasonal cycle of meridional currents off Angola, further south, and the  
 435 southward flow in February-March and October seems to be the Angola current (Kopte et al 2017). To  
 436 assess the zonal current (Fig.6c and 6d), we make a longitudinal section at 10°E and we look at the  
 437 seasonal cycle of zonal current between 3°S and 7°S. The modeled zonal structure with westward  
 438 velocities from April to August and November – December has a magnitude of about 0.1 m.s<sup>-1</sup> along  
 439 the section (Fig.6c), in agreement with the observations (Fig.6d), which also show westward velocities  
 440 from April to August. However there are some differences with the model from March to August  
 441 between 3°S and 4.5°S where we can observe very strong (more than 0.5 m.s<sup>-1</sup>) eastward flow. In  
 442 contrast to the model, the flow during November is eastward in the observation. The noticeable

443 similitude is the eastward flow in January- February and October with a magnitude of  $0.15 \text{ m}\cdot\text{s}^{-1}$  which  
 444 seems to be the signature of the South Equatorial UnderCurrent (SEUC). This eastward current is  
 445 deeper further offshore (100 m depth) west of  $0^\circ\text{E}$  (Bourles et al., 2004) and rising near the surface  
 446 near the coast (Nubi et al., 2016; Assene et al., 2022).

### 447 3.2 Nitrate budget in the mixed layer

448 Generally, the seasonal variations in CHLa are thought to be primarily related to seasonal variations of  
 449 the nitrate input in the equatorial Atlantic ocean (Loukos and Mémery., 1999; Radenac et al, 2020) and  
 450 in the tropical Angolan upwelling (Brandt et al., 2023). This is probably the case also in the  
 451 Gabon-Congo coastal area, where the seasonal cycles of nitrate (Fig.7a) and CHLa (Fig.5) in our  
 452 model are very consistent. Corresponding to the semi-annual variability of nitrate, the seasonal change  
 453 rate of its concentration (Fig. 8b) displays a four-phase cycle: a first increasing phase between March  
 454 and August with a highest amplitude ( $0.3 \text{ mmol}\cdot\text{m}^{-3}\cdot\text{d}^{-1}$ ) in July, followed by a decreasing phase in  
 455 September –November with a highest amplitude in October ( $0.01 \text{ mmol}\cdot\text{m}^{-3}\cdot\text{d}^{-1}$  north of  $5^\circ\text{S}$  and about  
 456  $-0.13$  to  $-0.3 \text{ mmol}\cdot\text{m}^{-3}\cdot\text{d}^{-1}$  between  $5^\circ\text{S}$  and  $6^\circ\text{S}$  all years long).

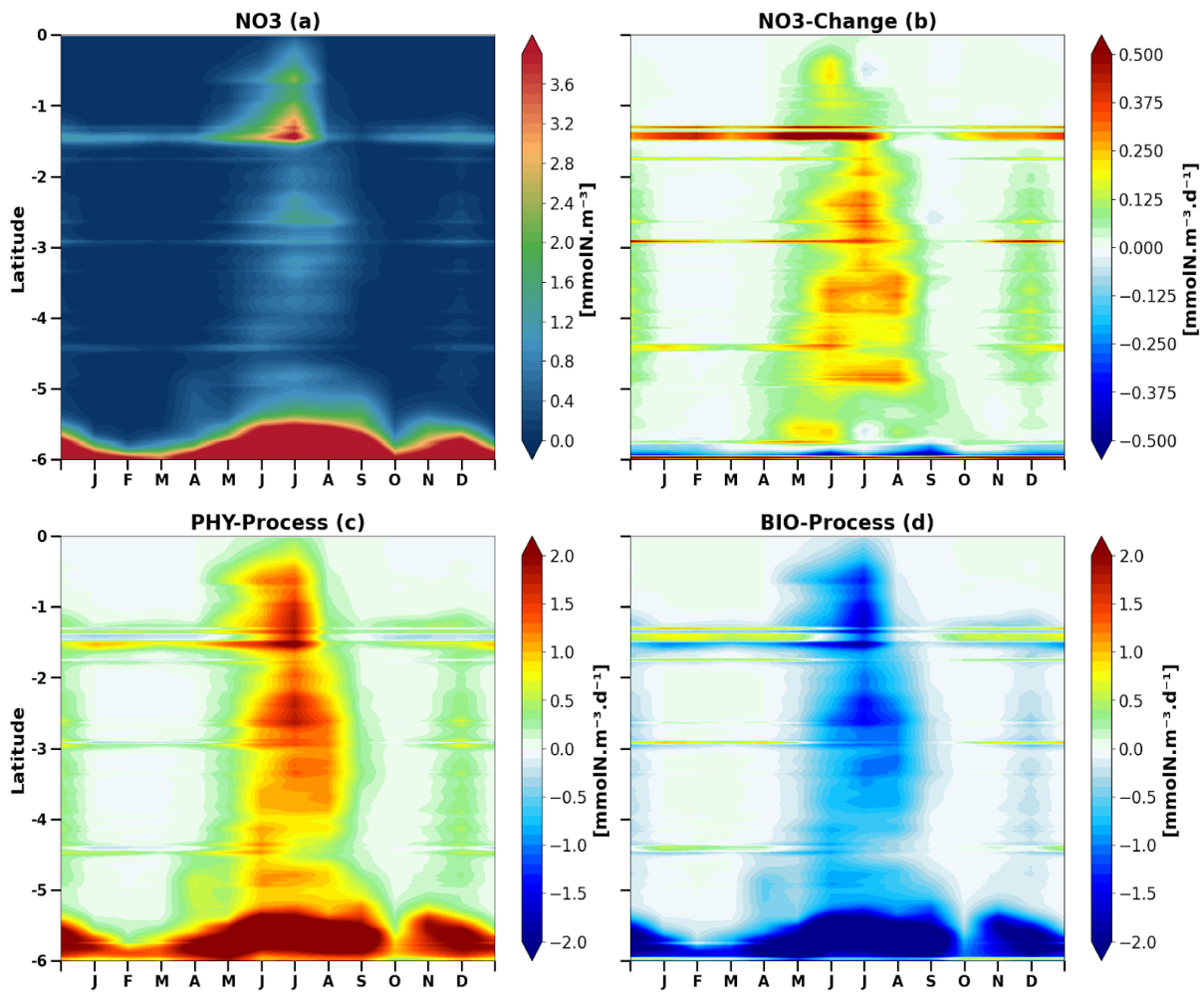


457  
 458 **Figure 6:** Seasonal cycle of surface current, zonal current (a, b) at  $10^\circ\text{E}$  section and between  $3^\circ\text{S}$  and  $7^\circ\text{S}$   
 459 meridional current (c, d) at  $4^\circ\text{S}$  section from  $7^\circ\text{E}$  to the coast.

460 Then we have a weak second increasing phase in November-December of about  $0.1 \text{ mmol.m}^{-3}.\text{d}^{-1}$  and a  
 461 weak decreasing phase in January- February ( $0.01 \text{ mmol.m}^{-3}.\text{d}^{-1}$ ). This semi-annual cycle is due to a  
 462 balance between nitrate supply by physical processes (Fig.7c), maximum during the main upwelling  
 463 period, and nitrate consumption by biological processes (Fig.7d).

### 464 3.2.1 Seasonal Nitrate Budget Analysis: Horizontal Vs Vertical Contributions

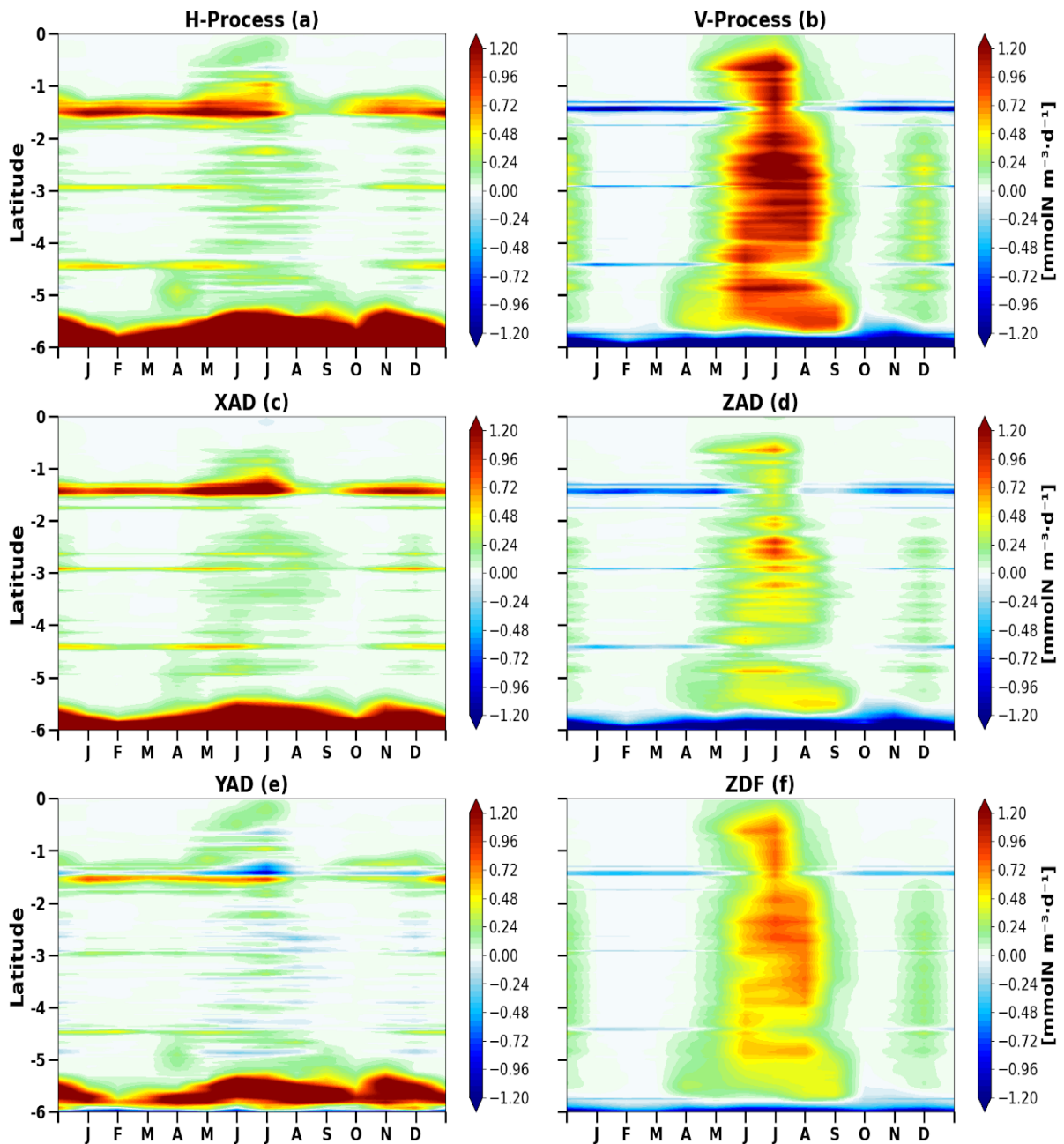
465 Looking at our previous results, we saw that physical processes drive the nitrate supply in the  
 466 Gabon-Congo upwelling system, now we will look at the contribution of horizontal and vertical  
 467 processes to understand which are the main drivers for this nitrate supply. Fig.8 shows that horizontal  
 468 and vertical processes (Fig.8a and Fig.8b respectively) are of great importance for nitrate supply.



469 **Figure 7:** Latitude-time Hovmöller diagram of the model seasonal cycle of Mixed Layer Nitrate (MLN) budget,  
 470 a), the rate of the MLN change (b), the physical process contribution (c) and the biological process contribution  
 471 d) along the Gabon-Congo coast. Units are  $\text{mmolN.m}^{-3}$  and  $\text{mmolN.m}^{-3}.\text{d}^{-1}$  for Figure 7a and Figure 7b,c,d,  
 472 respectively.

474 In fact, as we can see in the Fig.8, vertical processes (Fig.8b) are the main driver of nitrate supply  
 475 during the upwelling between  $0^{\circ}\text{S}$  and  $5.5^{\circ}\text{S}$  with an input magnitude of around  $1 \text{ mmol.m}^{-3}.\text{d}^{-1}$  along  
 476 the coast while the horizontal processes are the main driver at the vicinity of Congo river mouth ( $5.5^{\circ}\text{S}$

477 – 6°S) all year long. The latter seems to be dominated by zonal advection (fig.8c) with a very high  
478 nitrate input of more than  $1.2 \text{ mmolN.m}^{-3}.\text{d}^{-1}$  nearby 6°S with a northward extension, largest firstly in  
479 November-December and secondly in June-July. This is consistent with the seasonal maximum of  
480 Congo River discharge, which suggests a nitrate input through the river plume (Hopkins et al 2013).  
481 North of 6°S, meridional advection (Fig.8e) drives horizontal processes.  
482 The nitrate budget analysis reveals also that vertical processes (Fig.8b) are dominated by vertical  
483 mixing (Fig.8f), while vertical advection has the same seasonality but a smaller contribution (Fig.8d).  
484 Indeed, the nitrate input by the vertical diffusion is about  $0.7 \text{ mmolN.m}^{-3}.\text{d}^{-1}$  but only around  $0.5$   
485  $\text{mmolN.m}^{-3}.\text{d}^{-1}$  by vertical advection. Both vertical processes decrease nitrate concentration nearby  
486 6°S, under Congo River plume influence with the dominant zonal advection contribution. Indeed, as  
487 nitrate concentration is greater in the near-surface Congo River plume than in subsurface (between 5 to  
488 10 m, see Fig.3), deeper waters rising at the surface by vertical advection reduce nitrate in the plume  
489 area.



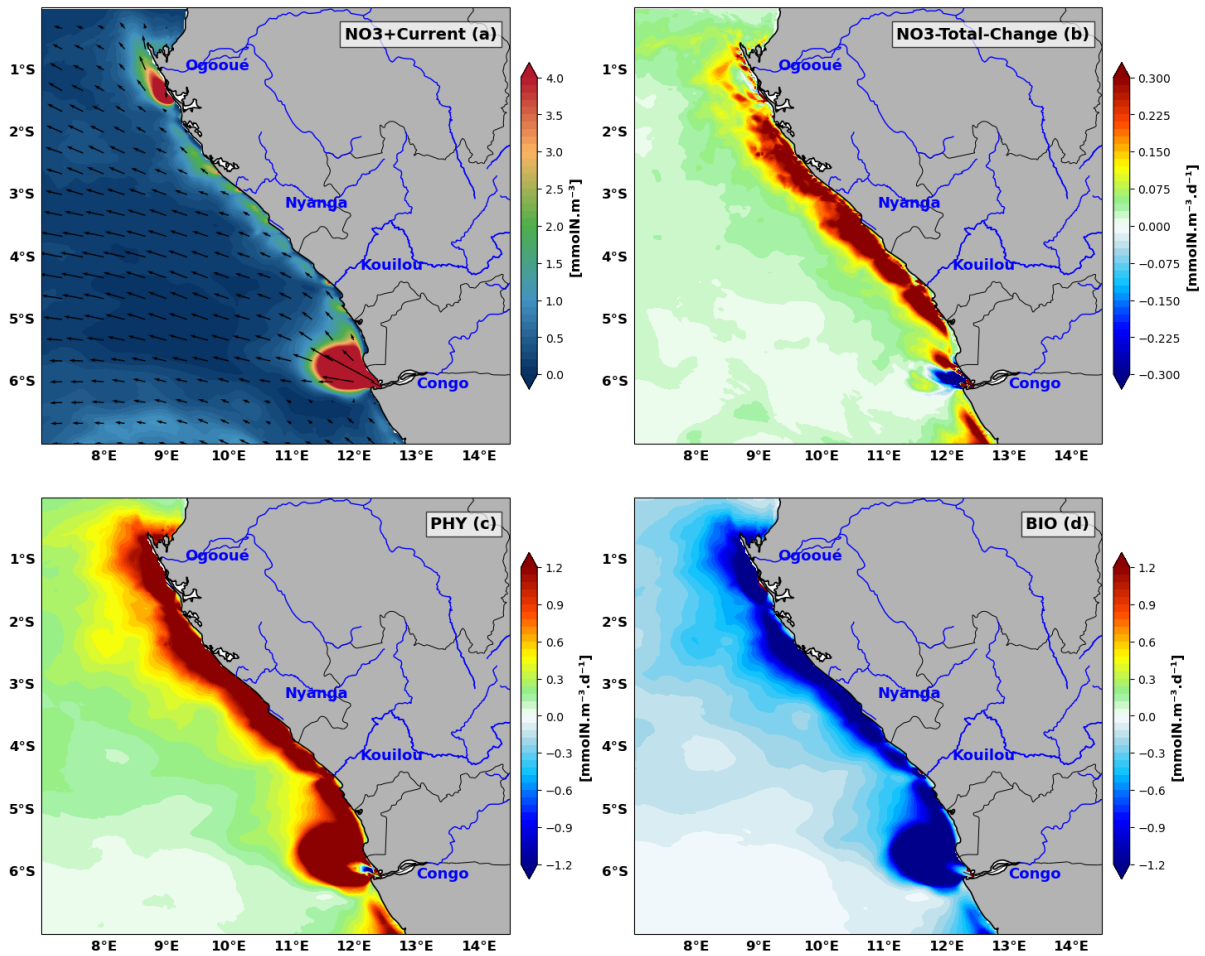
490

491 **Figure 8:** Latitude-time Hovmöller diagram of the model seasonal cycle of horizontal (a) and vertical (b) process  
 492 contributions , zonal (c), meridional (e), vertical (d) advctions , vertical diffusion (f) averaged in the mixed  
 493 layer along the Gabon-Congo coast. Units are  $\text{mmolN.m}^{-3}.\text{d}^{-1}$ .

494 Similarly, vertical mixing of subsurface waters with the plume waters decreases nitrate concentration  
 495 at the surface, although the strong haline stratification associated with the Congo River plume limits  
 496 this effect.

497 It is important to note that, on the one hand, vertical advection (Fig. 8d) and vertical diffusion (Fig. 8f)  
 498 have the same seasonality as SLA (Fig. 4a), in opposite phase, northward of  $5.5^{\circ}\text{S}$ . This suggests that  
 499 the upwelling associated with CTWs (negative SLA) induce these vertical processes and therefore  
 500 drive the input of nitrate in the northern part of the Gabon-Congo coast. On the other hand, horizontal  
 501 advection (both zonal and meridional advctions) has the same seasonality as the Congo River

502 discharge between 5.5°S and 6°S. This suggests that the Congo River supplies nitrate through zonal  
 503 advection, near its mouth.



504

505 **Figure 9:** Spatial distribution averaged over the main upwelling period of (a) nitrate, (b) nitrate tendency  
 506 contributed by (c) physical processes and (d) biological processes, all averaged in the mixed layer in Austral  
 507 winter. The mean current in the mixed layer is superimposed in (a). Nitrate concentration units are  $\text{mmolN}\cdot\text{m}^{-3}$   
 508 and the tendency terms units are  $\text{mmolN}\cdot\text{m}^{-3}\cdot\text{d}^{-1}$ .

### 509 3.2.2 Regional Nitrate Budget Analysis in the main upwelling period: Physical Vs 510 Biological Contributions

511 The regional distribution of nitrate balance terms averaged over the mixed layer for the austral winter  
 512 (June-July-August), when upwelling reaches its maximum intensity, is presented in Fig.9. The nitrate  
 513 tendency (Fig.9b) shows that during the upwelling period, nitrate input occurs throughout the domain  
 514 with values varying between  $-0.3$  to  $0.3 \text{ mmolN}\cdot\text{m}^{-3}\cdot\text{d}^{-1}$  in the plume zone and  $0.2$  to  $0.56$   
 515  $\text{mmolN}\cdot\text{m}^{-3}\cdot\text{d}^{-1}$  along the coast in the northern part. In the offshore zone, the nitrate tendency is lower,  
 516 with a magnitude of around  $0.05 \text{ mmolN}\cdot\text{m}^{-3}\cdot\text{d}^{-1}$ . This distribution of the nitrate tendency shows that  
 517 the input of nitrate by physical processes (Fig.9c) is slightly greater than the uptake of nitrate by  
 518 biological processes (Fig.9d) throughout the area, explaining the positive nitrate change rate, except at

519 the Congo River mouth where we have negatives values . Fig.9a shows that nitrate inputs along the  
520 coast are very high close to river mouth and varies a lot along the coast over a width of about 165 km  
521 from the coast. During this main period of upwelling, in general, vertical processes (Fig. 10b) largely  
522 dominate the nitrate supply across the entire continental shelf. A continuous coastal band of strong  
523 enrichment is observed, with values often exceeding 0.513 to 0.677  $\text{mmolN.m}^{-2}.\text{d}^{-1}$ . Conversely,  
524 horizontal processes (Fig. 10a) show a more localized and overall lower contribution throughout the  
525 domain, with the notable exception of the Congo and Ogooué River mouth ( $\sim 6^{\circ}\text{S}$  and  $1^{\circ}\text{S}$   
526 respectively), where a massive positive flux (dark red,  $> 0.677 \text{ mmolN.m}^{-2}.\text{d}^{-1}$ ) is observed.  
527 Comparing the spatial structure of the total horizontal process (Fig. 10a) with its individual  
528 components reveals a striking similarity to zonal advection (Xad, Fig. 10c). The Xad signal (Fig. 10c)  
529 almost perfectly reproduces the nitrate patch observed at the Congo mouth, indicating that zonal  
530 transport (east-west) is the main driver of horizontal nitrate injection into the mixed layer, associated  
531 with the offshore extension of the river plume. Although meridional advection (Yad, Fig. 10e) exhibits  
532 significant dipole structures near the Congo and patches along the coast, its intensity and spatial  
533 pattern provide a less compelling explanation for the overall horizontal process signal. It can therefore  
534 be concluded that zonal advection is the dominant term dictating the distribution of horizontal fluxes  
535 in this region. The study of vertical components shows that the total vertical process (Fig. 10b) results  
536 from two distinct yet complementary mechanisms. Vertical advection (Zad, Fig. 10d) shows very  
537 intense ( $> 0.677 \text{ mmolN.m}^{-2}.\text{d}^{-1}$ ) but highly localized supply along the coastline and capes,  
538 representing the typical signature of coastal upwelling driven by wind and Coastally Trapped Waves  
539 (CTWs). However, vertical diffusion (Zdf, Fig. 10f) shows the strongest resemblance to the overall  
540 Vert\_Process. It exhibits a broad and homogeneous distribution extending well offshore from the coast,  
541 with sustained values between 0.349 and 0.513  $\text{mmolN.m}^{-2}.\text{d}^{-1}$ . Unlike advection, which is highly  
542 segmented, vertical diffusion better explains the spatial continuity of nitrate supply across the shelf.  
543 This suggests that while advection (upwelling) brings nitrate to the base of the mixed layer, turbulent  
544 mixing (diffusion) ensures its effective distribution toward the surface across the entire domain.

### 545 3.3 Nitrate budget in the euphotic layer and along the water column

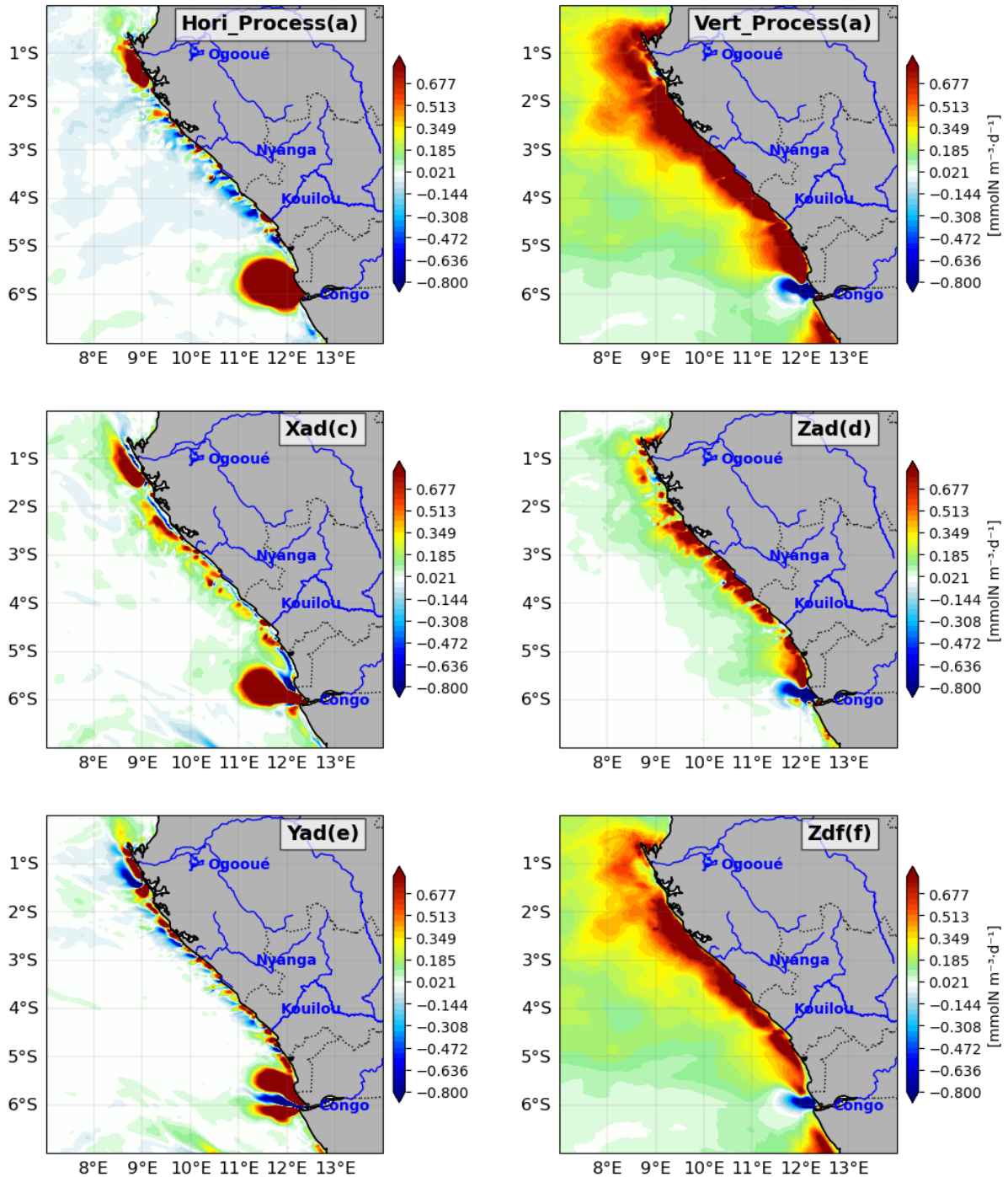
546 Now, in addition to the processes acting in the surface mixed layer, we investigate other processes  
547 involved in the nitrate budget below the mixed layer by analysing the nitrate budget in the euphotic  
548 layer, generally defined as the zone where light penetration exceeds 1% of the surface light, allowing  
549 for the presence of phytoplankton and other photosynthetic organisms. The seasonal variations of  
550 thermocline, mixed layer and euphotic layer depths are compared in Fig.11. In Fig.11a, the  
551 thermocline ( $20^{\circ}\text{C}$  isotherm) variation is very close to the nitracline as suggested by Radenac et al  
552 (2020). The mixed layer euphotic layer is very shallow ( $\sim 10 \text{ m}$ ) throughout the year probably due to  
553 the Congo River plume stratification. The euphotic layer extends deeper than the mixed layer, but is  
554 generally shallower than the thermocline, except from June to September. The euphotic layer gets

555 thinner during upwelling through the enhancement of CHLa concentration which reduces light  
556 penetration (self-shadowing by CHLa). Overall the nitrate tendency (Fig.11b) has the same  
557 semi-annual variation in the euphotic layer than in the mixed layer, although more intense in the  
558 euphotic layer with a maximum at the bottom of the euphotic layer. In fact, most nitrate input by  
559 physical processes (Fig.11c) happens in the mixed layer, where it is almost balanced by biological  
560 nitrate uptake (Fig.11d). In contrast, in the euphotic layer below the mixed layer (between 10m and  
561 40m depth), biological processes are poorly active and the nitrate variability is almost exclusively  
562 induced by physical processes. The mean nitrate input in the euphotic layer is about  $0.1 \text{ mmolN.m}^{-3}.\text{d}^{-1}$   
563 during the main upwelling period and the maximum input ( $0.2 \text{ mmolN.m}^{-3}.\text{d}^{-1}$ ) occurs in May at the  
564 base of the euphotic layer (Fig.11b).

565 In the euphotic layer, biological activity is dominated by photosynthesis which removes nitrate,  
566 whereas below the euphotic layer remineralization supplies nitrate with about  $0.05 \text{ mmolN.m}^{-3}.\text{d}^{-1}$   
567 almost all year long (Fig. 11d).

### 568 3.3.1 Euphotic Layer Nitrate Budget Analysis: Horizontal Vs Vertical Contributions

569 Fig.12 shows that, even in the euphotic layer, the physical contribution to nitrate supply (Fig.11c) is  
570 mostly driven by vertical processes (Fig.12b). However, the large decrease in nitrate (Fig.11b) in  
571 October is also caused by horizontal contributions (Fig.12a) in the euphotic layer. Between the surface  
572 and 5m depth, horizontal processes dominate nitrate input (Fig.12e). In the euphotic layer below,  
573 meridional advection is the main driver of nitrate removal almost year-round, particularly in June and  
574 October.

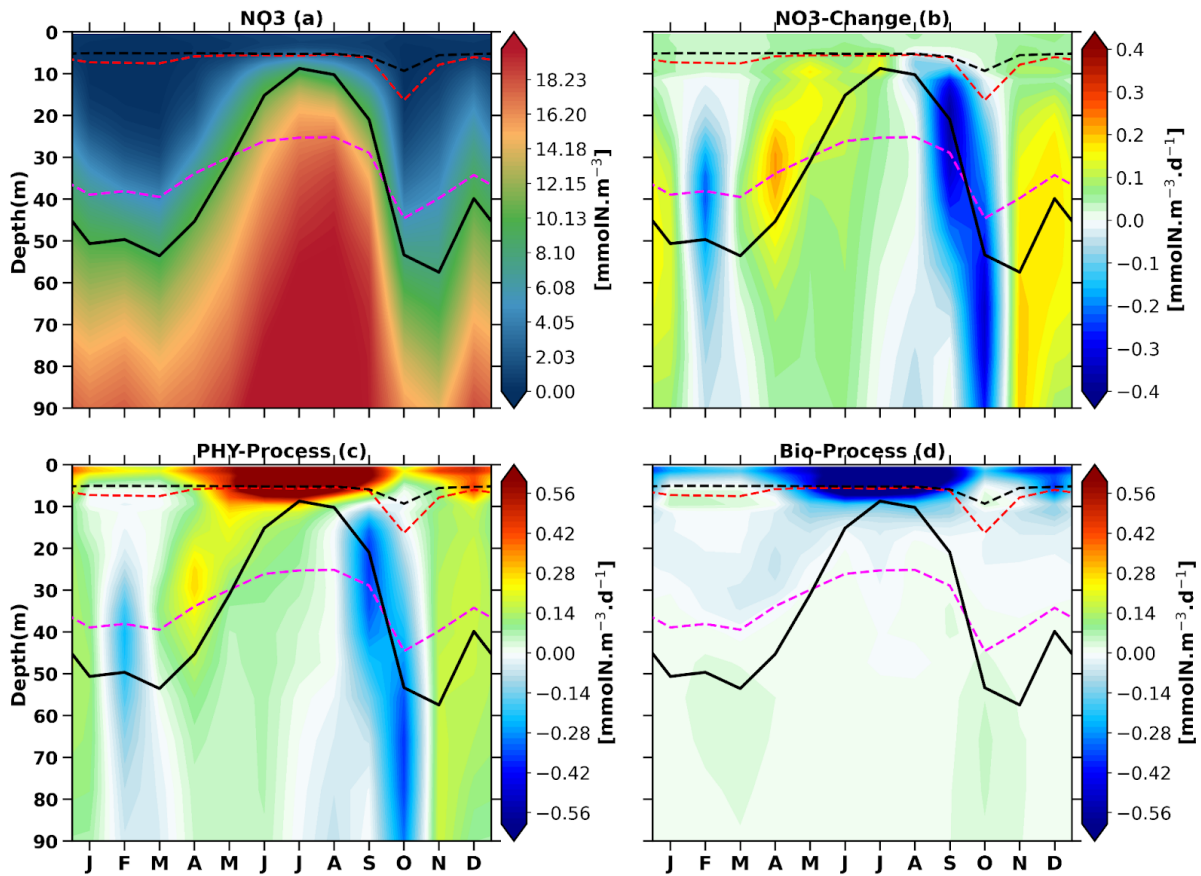


575

576 **Figure 10:** Contribution of (a) the horizontal processes, including (c) zonal advection and (e) meridional  
 577 advection, and (b) vertical processes, including (d) vertical advection and (f) vertical diffusion, to the nitrate  
 578 budget averaged in the mixed layer during the austral winter. Units are  $\text{mmolN.m}^{-3}.\text{d}^{-1}$ .

579 Zonal advection (Fig.12c) supplies nitrate in the euphotic layer, with a maximum above the mixed  
 580 layer depth, throughout the year. This nitrate input is more than compensated by nitrate lost by  
 581 meridional contribution, below the upper 5 m (Fig.12e), except in June, July and August. Vertical  
 582 advection (Fig.12d) is the dominant vertical process (Fig.12b) in the nitrate budget. Below 30 m depth,  
 583 it has a semi-annual cycle characteristic of upwelling and downwelling CTWs propagation, associated

584 with nitrate increase when the thermocline shallows and nitrate decrease when the thermocline  
 585 deepens, with the maximum and minimum values around the thermocline depth. Moreover, vertical  
 586 advection supplies more nitrate in the mixed layer than in the euphotic layer below during the main  
 587 upwelling period (June, July and August), but rather the opposite during the second upwelling period  
 588 (December). Between the mixed layer depth and the euphotic layer depth, vertical diffusion (Fig.12f)  
 589 tends to partially compensate for the effects of vertical advection on nitrate. However, in the mixed  
 590 layer it mostly supplies nitrate, particularly during the upwelling seasons.



591

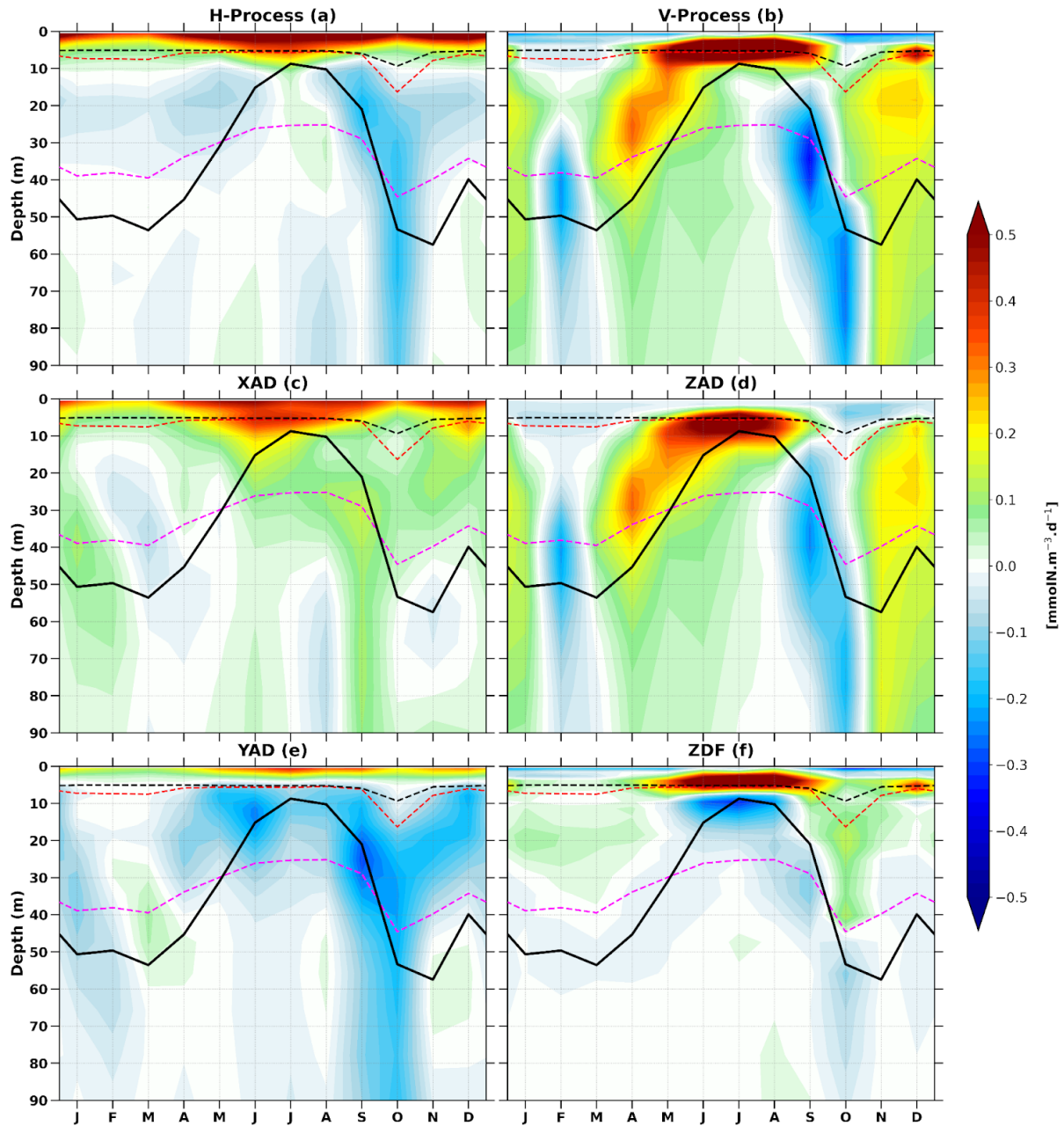
592 **Figure 11:** Depth-time Hovmöller diagram of the seasonal cycle of the nitrate budget averaged within the  
 593 Gabon-Congo coastal box ( $0^{\circ}\text{S}$ – $6^{\circ}\text{S}$ ,  $1^{\circ}$  wide coastal band, as shown in Fig. 1). (a) Nitrate concentration  
 594 ( $\text{mmolN.m}^{-3}$ ), (b) nitrate rate of change, (c) physical process contribution, and (d) biological process  
 595 contribution ( $\text{mmolN.m}^{-3}.\text{d}^{-1}$ ). The black solid line represents the thermocline ( $20^{\circ}\text{C}$  isotherm), while dashed  
 596 magenta, red and black lines indicate the euphotic, isothermal and mixed layer depths, respectively.

### 597 3.3.2 Nitrate budget analysis: advection components analysis

598 As nitrate advection depends on velocity and on the nitrate gradient, we now evaluate the individual  
 599 contributions of seasonal variations in velocity and nitrate gradient, as well as their combined effect, to  
 600 the seasonal variations of nitrate advection (see section 2.3, equation 4).

#### 601 3.3.2.1 horizontal advection

602 Fig.13 allows to visually compare the depth-time structure of the zonal nitrate advection (Fig.13a)  
 603 with that of its different components, while correlation  $r$  is used to quantify the comparison.

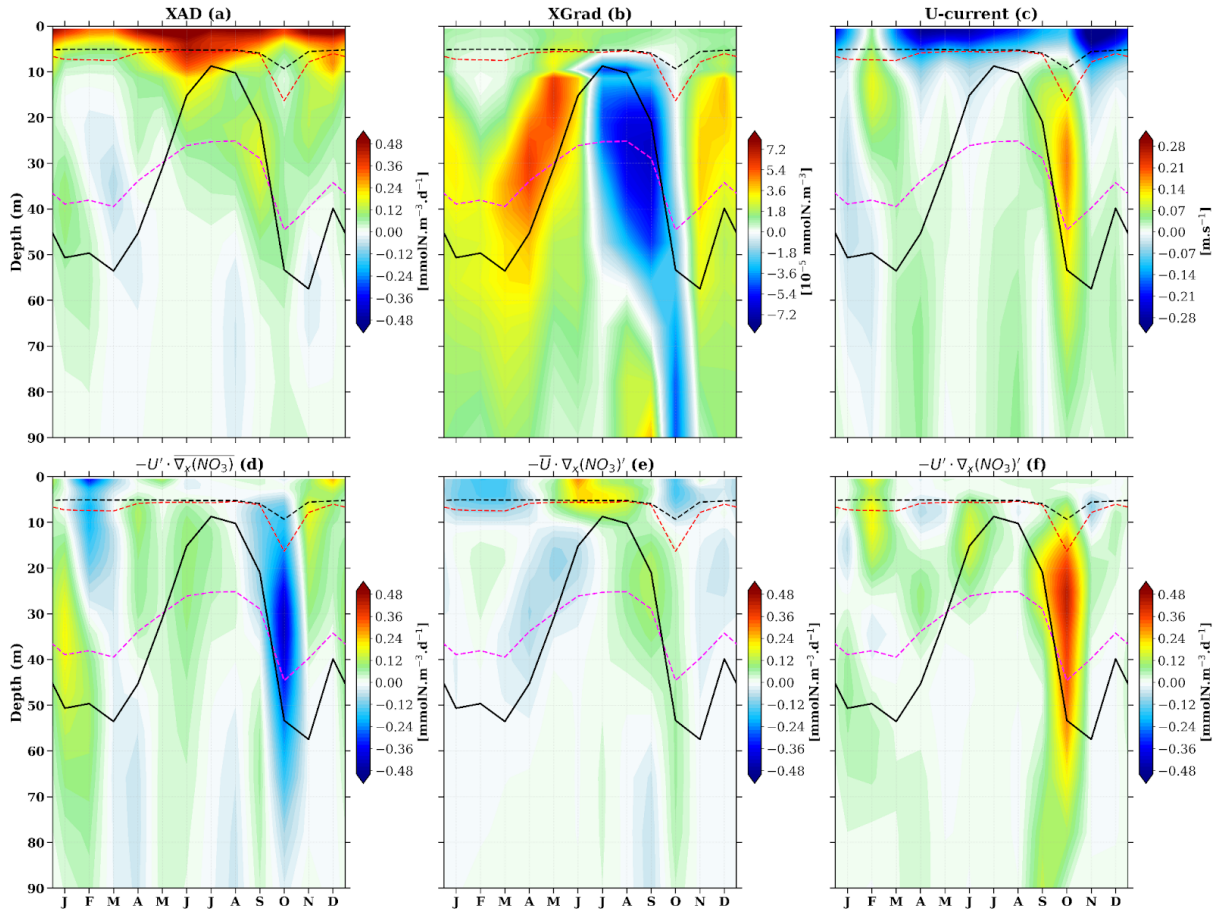


604

605 **Figure 12:** Depth-time Hovmöller diagram of the model seasonal cycle of contributions to the nitrate budget of  
 606 horizontal and vertical processes (a and b respectively), zonal, meridional, vertical advections (c, e and d  
 607 respectively), vertical diffusion (f) along the Gabon-Congo coast (0°S-6°S and 1° width to the coast). Units are  
 608  $\text{mmolN.m}^{-3}$  for all of the plots. The black solid line represents the thermocline (20°C isotherm), while dashed  
 609 magenta, red and black lines indicate the euphotic, isothermal and mixed layer depths, respectively.

610 The seasonal cycle of zonal nitrate advection in the 0-100 m water column (Fig. 13a) is controlled first  
 611 by the term  $\overline{u \cdot \nabla x(NO_3)}$  (Fig.13e,  $r=0,77$ ,  $p<0,05$ ), i.e. the annual mean zonal current multiplied by  
 612 the seasonal variations of the nitrate zonal gradient, second by the term  $u \cdot \overline{\nabla x(NO_3)}$ , (Fig.13d,  $r=0,49$ ,  
 613  $p<0,05$ ), i.e. the seasonal variations of the zonal current multiplied by the annual mean nitrate zonal  
 614 gradient, and third (and much less) by the term. The third component, which represents the

615 simultaneous variation in zonal current and nitrate gradient  $u' \cdot \nabla_x(NO_3)'$ , (Fig.13f,  $r=-0,15$ ,  $p<0.05$ ),  
 616 i.e. the product of seasonal variations of both the zonal current and the nitrate zonal gradient. The  
 617 seasonality of the zonal current (Fig. 13c) is influenced by the seasonal cycle of the South Equatorial  
 618 Undercurrent (SEUC), with maximum values in September-October and February-March (Dorothee et  
 619 al, 2004) in this zone ( $0^\circ\text{S}-6^\circ\text{S}$ ,  $1^\circ$  from the coast). Thus we can conclude that the SEUC plays a key  
 620 role in the nitrate balance in the Gabon-Congo system by bringing nitrate in February-March and in  
 621 September-October to the euphotic layer.



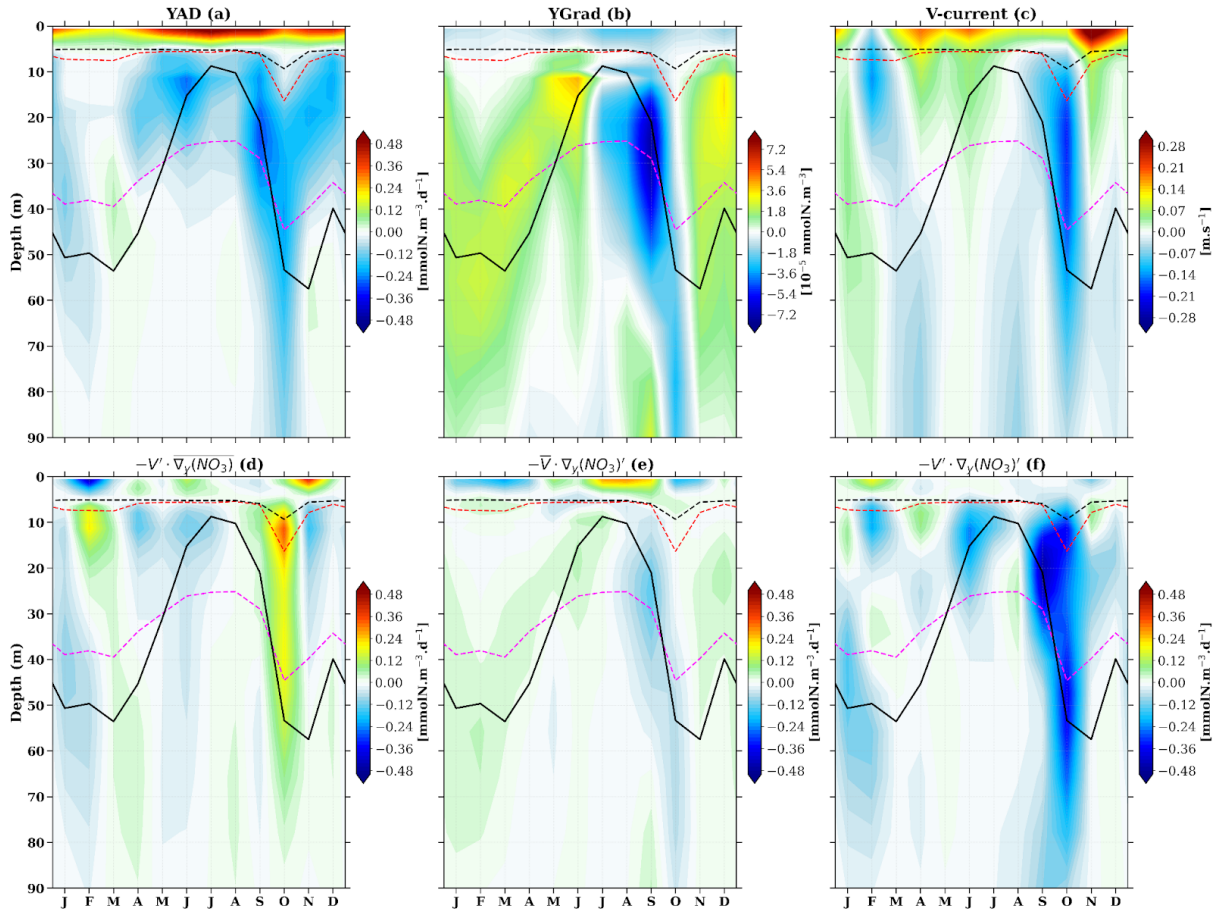
622 **Figure 13:** Depth-time Hovmöller diagram of the model seasonal cycle of nitrate advection (a), nitrate gradient  
 624 (b), zonal current (c), zonal current variation times mean nitrate gradient (d), gradient variation times mean  
 625 current (e) and gradient variation times zonal current variation (f), all along the zonal axis in the Gabon-Congo  
 626 coastal box of Fig. 1. Units are milli mol per cubic meter per day for all of the plots except (b) (milli mol per  
 627 cubic meter) and (c) (meter per second). The black solid line represents the thermocline ( $20^\circ\text{C}$  isotherm), while  
 628 dashed magenta, red and black lines indicate the euphotic, isothermal and mixed layer depths, respectively.

629 In the euphotic layer, we see that, as for the meridional nitrate advection, the meridional current  
 630 (Fig.14c) looking at the shape seems to be the main factor in the vertical and temporal variation shape  
 631 of the meridional nitrate advection (Fig.14a). The Angola current (AC), is the factor which modulates  
 632 nitrate lost by meridional nitrate advection throughout the year, with maximum loss in  
 633 September-October and June-July, in and below the euphotic layer, except in the first 5 m-depth.

634 Our analysis in this section reveals that the simultaneous variation in both the meridional current and  
635 the gradient ( $v' \cdot \nabla_y(NO_3)$ ), Fig.14f) exhibits the highest correlation ( $r=0.527$ ,  $p<0.05$ ) with meridional  
636 nitrate advection, thus explaining the major changes in advection. This result highlights the significant  
637 impact of the concurrent variability of both meridional current and gradient on meridional nitrate  
638 advection in the euphotic layer. In contrast, gradient variation ( $\overline{v \cdot \nabla_y(NO_3)}$ ), Fig.14e) is poorly  
639 correlated ( $r=0.97$ ,  $p<0.05$ ) with meridional nitrate advection. The very low positive correlation with  
640 total meridional advection (a) indicates this term, representing the effect of a mean meridional current  
641 acting on a fluctuating nitrate gradient. This suggests that either the mean meridional current is weak,  
642 or its interaction with the fluctuating gradient does not lead to significant changes in overall advection.  
643 The variation in the meridional current ( $v' \cdot \overline{\nabla_y(NO_3)}$ ), Fig.14d) shows the lowest correlation ( $r=0.287$ ,  
644  $p<0.05$ ). This low, negative correlation with total meridional advection (Fig.14a) indicates that this  
645 term, representing the effect of fluctuating meridional currents on a relatively stable mean nitrate  
646 gradient, is not a dominant driver of the overall meridional nitrate advection. In fact, a negative  
647 correlation suggests it might weakly oppose the main advection pattern or have an inverse relationship.  
648 This implies that the mean gradient is either small or the meridional current variations are not aligned  
649 to produce significant advection changes via this mechanism.

### 650 3.3.2.2 vertical processes

651 Our analysis reveals that within the euphotic layer, the variation in the vertical gradient  $\overline{w \cdot \nabla_z(NO_3)}$ ,  
652 Fig.15e) appears to better explain the variation in vertical nitrate advection (Fig.15a), showing a  
653 correlation of  $r=0.79$  ( $p<0.05$ ). In contrast, vertical velocity variation ( $w' \cdot \overline{\nabla_z(NO_3)}$ ), Fig.15d) plays a  
654 secondary role, with a correlation of approximately 0.646 ( $p<0.05$ ) with vertical nitrate advection.  
655 Looking now at the vertical nitrate advection, we can see strong similarities in the vertical and  
656 temporal variation structure between vertical advection seasonality (Fig.15a), vertical nitrate gradient  
657 seasonality (Fig.15b) and vertical velocity seasonality (Fig.15c), both three are very strong in the  
658 euphotic layer. We can also see in the semi-annual vertical velocity that from April to August and  
659 November-December, vertical velocities are upward corresponding to negative values of SLA (Fig.4a,  
660 4b), lowest SST (Fig.4c, 4d) values and highest nitrate concentration (Fig.4e, 4f). From January to  
661 March and September-October, vertical velocities are downward corresponding to positive values of  
662 SLA (Fig.4a, 4b), highest SST (Fig.4c, 4d) values and lowest nitrate concentration (Fig.4e, 4f). This  
663 later observation confirms that CTWs propagating from April to August and November-December are  
664 associated with upwelling. In contrast, CTWs propagating from January to March and  
665 September-October are associated with downwelling. Note that similar results were found by Ngakala  
666 et al. (2025) for the seasonal heat budget in the Gabon-Congo upwelling (from 4°S-6°S and 1° width  
667 to the coast) and also further south in the Angolan upwelling by Korner et al. (2024).



668

669 **Figure 14:** Depth-time Hovmöller diagram of the model seasonal cycle of nitrate advection (a), nitrate gradient  
 670 (b), meridional current (c), meridional current variation times mean nitrate gradient (d), gradient variation times  
 671 mean meridional current (e) and gradient variation times current variation (f), all along the meridional axis in the  
 672 Gabon-Congo coastal box of Fig. 1b. Units are milli mol per cubic meter per day for all of the plots except (b)  
 673 (milli mol per cubic meter) and (c) (meter per second). The black solid line represents the thermocline (20°C  
 674 isotherm), while dashed magenta, red and black lines indicate the euphotic, isothermal and mixed layer depths,  
 675 respectively.

676 However, if we average in the first hundred meters, vertical velocity variation has the highest  
 677 correlation of 0.831 ( $p < 0.05$ ) with vertical advection, whereas vertical gradient variation has only 0.63  
 678 ( $p < 0.05$ ) of correlation with vertical advection. The third component ( $w' \cdot \nabla_z(NO_3)'$ ), Fig.15f) has a  
 679 lower negative correlation -0.062 ( $p < 0.05$ ) with vertical advection. During the upwelling period, the  
 680 variation in vertical gradient (Fig.15e) at the base of the mixed layer has a much greater influence on  
 681 nitrate supply than the variation in vertical velocity (Fig.15e). Another observation is that in the same  
 682 main upwelling period there is a lag between maximum vertical current which happens in May and the  
 683 maximum vertical gradient indicated by the shallowest thermocline in July. This lag results in a  
 684 highest input of nitrate by vertical advection (Fig.15a) in the mixed layer in June. It can be seen that  
 685 the nitrate output by vertical advection during the downwelling period is mostly induced by the

686 vertical nitrate gradient in the mixed layer whereas deeper in the euphotic layer these losses are  
687 induced by vertical downward velocities induced by downwelling CTWs propagation.

#### 688 **4 Discussion**

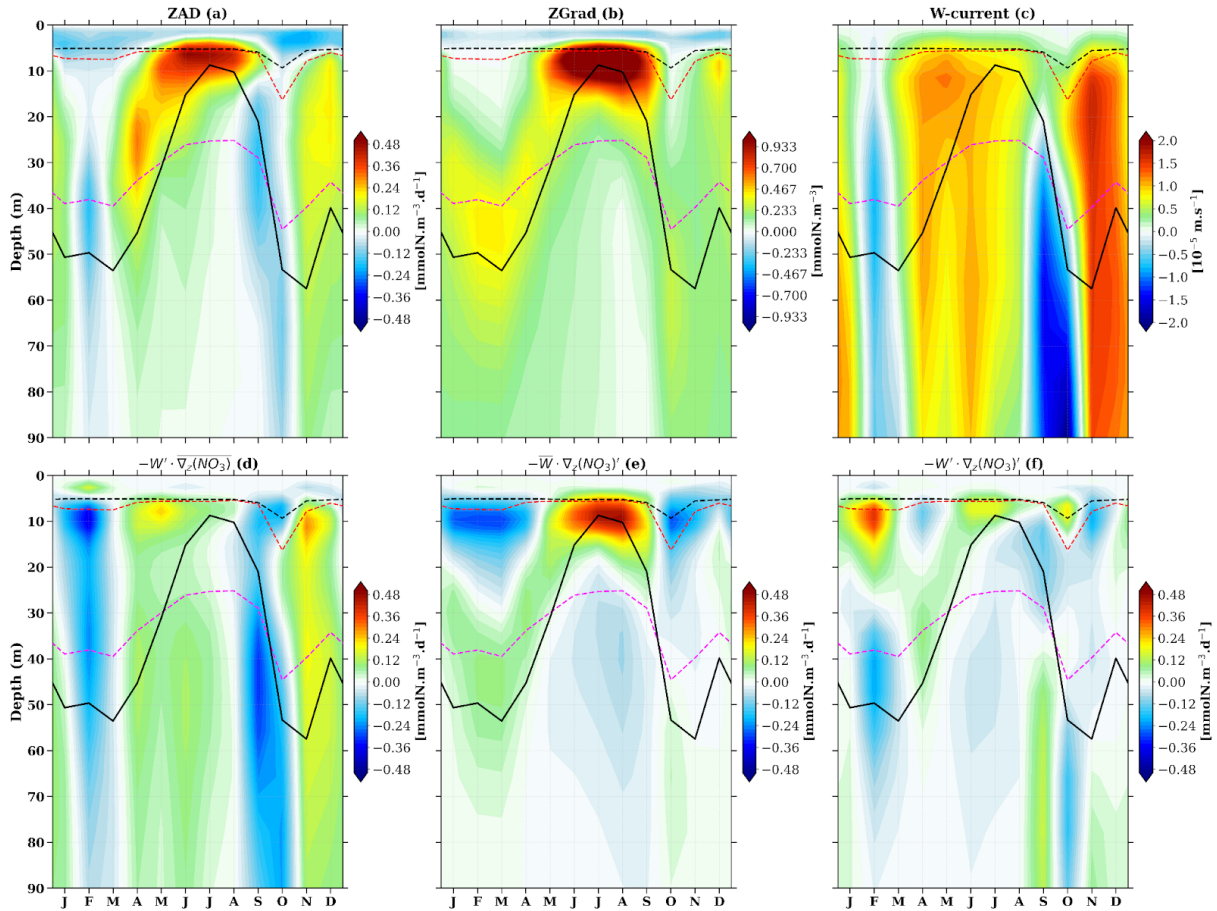
689 In this section, we discuss our results: the model-data comparison, the influence of the mixed layer  
690 criteria, the main nitrate budget drivers in the Gabon-Congo upwelling system compared to the other  
691 tropical Atlantic upwelling systems. Finally, we will explore the factors governing seasonal  
692 productivity in the Gabon-Congo upwelling system, integrating our understanding of physical forcing  
693 and nutrient availability to characterize its biological response. Through this comprehensive  
694 discussion, we aim to provide a nuanced understanding of the oceanographic processes at play in the  
695 coastal Congo region and the capabilities and limitations of our modeling approach.

696 Throughout this work, we have shown that our model reasonably reproduces the observations in terms  
697 of temperature, nitrate, CHLa, SLA and surface currents, although there are a few differences that we  
698 will discuss in this section. First of all, we saw that temperature in our model is warmer than observed  
699 by around 1°C in regional distribution (Fig. 2a,b) as well as in seasonal cycles (Fig. 4c,d). This is a  
700 common bias in ocean and climate models in the Eastern tropical Atlantic (Richter, 2015; Zuidema et  
701 al., 2016; Voltaire et al., 2019). Indeed, several studies suggest that this warm bias is multicausal.  
702 While it is partly attributed to models' deficiency in simulating low-level clouds, resulting in  
703 overestimation of shortwave radiation (Xu et al., 2014), other factors play a critical role. These include  
704 errors in atmospheric forcing, specifically the misrepresentation of the coastal low-level jet and wind  
705 stress, which can weaken coastal upwelling (Cabos et al., 2017; Voltaire et al., 2019). Furthermore,  
706 complex air-sea feedback mechanisms (Koseki et al., 2018) and difficulties in simulating the vertical  
707 thermocline structure in the region (Koubanova et al., 2018) are also shared challenges that contribute  
708 to this persistent modeling bias.

709

710

711



712

713 **Figure 15:** Depth-time Hovmöller diagram of the model seasonal cycle of nitrate advection (a), nitrate gradient  
 714 (b), vertical current (c), vertical current variation times mean nitrate gradient (d), gradient variation times mean  
 715 vertical current (e) and gradient variation times current variation (f), all along the vertical axis in the  
 716 Gabon-Congo coastal box of Fig. 1b. Units are milli mol per cubic meter per day for all of the plots except (b)  
 717 (milli mol per cubic meter) and (c) (meter per second). The black solid line represents the thermocline (20°C  
 718 isotherm), while dashed magenta, red and black lines indicate the euphotic, isothermal and mixed layer depths,  
 719 respectively.

720 With regard to nitrate concentrations, the regional distribution shows that north of the mouth of the  
 721 Congo River and near the coast, the model agrees well with the CARS climatology (Fig. 2c,d).  
 722 However, offshore and south of the mouth of the Congo River, the model underestimates nitrate  
 723 concentrations. In the seasonal cycle, we see that the model captures the seasonal variability, but  
 724 underestimates the amplitude compared to the data. These biases may be explained by the temporal  
 725 coverage of the CARS climatology, which covers a long period (from 1940 to 2011) of data  
 726 (Bachelery et al., 2016) compared to our model which covers only one year (2011). Another bias may  
 727 be the lack of data in CARS, in our study area. The differences in the surface CHLa concentration  
 728 between the model and the satellite observations may be associated with a lack of data for the ocean  
 729 colour satellite observations, particularly in August, due to the cloud cover which induces atmospheric  
 730 contaminations (Hardman-Mountford and McGlade., 2002; Estival et al., 2013) of the satellite signal,

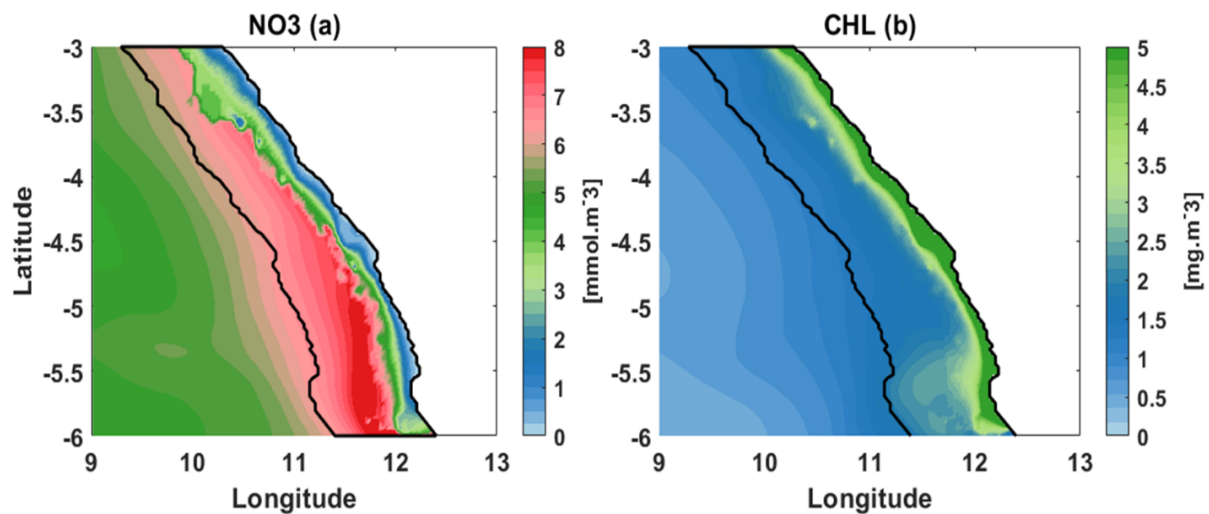
731 resulting in a lack of CHLa signal (Nieto et al., 2016). The biases in the surface currents between the  
732 model and the observations are mainly due to the underestimation of the currents in the OSCAR  
733 product near the coastal zone (Sikhakolli et al., 2013), especially in our studied area where very few  
734 data are available. Despite these results discussed earlier in this paper, we have to keep in mind that  
735 there are also some limitations in our simulation. For example, the model has difficulties reproducing  
736 the seasonal cycle of CHLa concentration, in particular the first CHLa blooms occurring in  
737 February-March, highlighted by the MODIS ocean colour satellite data. This might be due to the  
738 CHLa concentration of the Congo river in our model. Indeed, we take into account the nutrients and  
739 dissolved organic matter discharges of the river but not the CHLa concentrations (information not  
740 available in the HYBAM database). We can also observe a minimal or slightly reduced concentration  
741 of CHLa around the mouth of the Congo River in our model (Fig. 2e). This is explained by the very  
742 high speed (greater than 2 m/s) of the Congo River current at its mouth in our model. This has resulted  
743 in the transport of CHLa produced by phytoplankton photosynthesis away from the mouth of the  
744 Congo River.

745 Our analysis shows that, in the Gabon-Congo upwelling system, the nitrate budget in the mixed layer  
746 is dominated by physical processes during the upwelling period (Fig. 7c), particularly vertical  
747 diffusion (Fig. 8f), while zonal advection and vertical mixing play a secondary role. In agreement to  
748 these latter results, Ngakala et al. (2025) using a high resolution simulation ( $1/36^\circ$ ) of NEMO in the  
749 Gabon-Congo upwelling, have shown through a mixed layer heat budget, that vertical diffusion was  
750 the main contributor of cooling during upwelling period in the mixed layer. They found that the  
751 vertical advection has a secondary role in cooling of the mixed layer. They state that, if defining  
752 instead the mixed layer depth with the Boyer-Montégut criterion, then vertical advection would play a  
753 greater role than vertical diffusion. Thus, as mentioned in our study and in agreement with Ngakala et  
754 al. (2025), the relative contributions of vertical advection and diffusion depend on the definition of the  
755 mixed layer depth.

756 Our analysis reveals that the seasonal variability of CHLa in our region is driven by the seasonal  
757 concentration of nitrate, as in other tropical Atlantic upwelling systems (Radenac et al., 2020).  
758 However different processes drive the seasonal cycle of nitrate and CHLa in the different tropical  
759 Atlantic upwelling systems. In the Equatorial Atlantic upwelling system, the seasonal cycle of nitrate  
760 and CHLa are driven by the wind stress and wind stress curl (Caniaux et al., 2011, Radenac et al.,  
761 2020). In the Tropical Angola Upwelling system, the main driver of these seasonal cycle are the CTWs  
762 as in our area with a main peak in austral winter (May-July) and a second peak in December-January.  
763 However vertical mixing plays also a key role in the Tropical Angola Upwelling system (Awo et al.,  
764 2022; Ostrowski et al., 2009; Körner et al., 2023) due to onshore propagating internal tide waves  
765 interacting with sloping topography (Brandt et al., 2023). In the upwelling systems of the equatorial  
766 Atlantic and tropical Angola, vertical mixing is the main driver of nitrate input to the mixed layer. This  
767 is due to local mechanisms that occur in these areas (local forcing), such as the intensification of the

768 vertical shear stress between the South Equatorial Current (SEC) and the Equatorial Undercurrent  
769 (EUC) at the equator (Jouanno., 2010, Radenac et al., 2020) and the dissipation of internal tide that  
770 interact with the continental shelf and produce turbulent mixing at the Angolan coast (Körner et al.,  
771 2023, Zeng et al., 2021, Brandt et al., 2023). In the Gabon-Congo system, we can suggest that the  
772 strong stratification induced by the discharge of the Congo River, which is the second largest river in  
773 the world, contributes to thinning the mixed layer, limiting the effect of mixing very close to the  
774 surface (Dossa et al., 2019).

775 In the euphotic layer and below, the nitrate budget is almostly dictated by physical processes, which  
776 are mainly modulated by currents that transport water of different properties. We noted that vertical  
777 and zonal advectons were the drivers of nitrate input in the upwelling period, while vertical mixing  
778 and meridional advection were the drivers of nitrate losses in the lower part of the euphotic layer (just  
779 below the mixed layer depth) in this period. However, during the downwelling period, vertical mixing  
780 mostly brings nitrate to the lower part of the euphotic layer, while vertical and meridional advection  
781 always remove nitrate. Meridional advection is therefore the main factor in nitrate loss in the euphotic  
782 layer all year long. This is consistent with the warming effect of meridional advection shown by  
783 Körner et al. (2023) in the Angolan upwelling. Radenac et al (2020) showed that in the equatorial  
784 euphotic layer, zonal advection by the EUC current was the main driver of nitrate losses, which may  
785 explain our previous results since the southward Angola current dominating the ocean circulation in  
786 the Congo-Angola zone is fed by the EUC current. Indeed, the EUC, whose source waters come from  
787 the oligotrophic layers of the subtropical South Atlantic, has relatively low nitrate concentrations  
788 compared to neighbouring waters (Schott et al., 1998; Johns et al., 2014; Tuchen et al., 2022a). These  
789 low nitrate waters are brought to the Congo-Angola system by the Angola Current (AC) (Fig.16),  
790 reducing nitrate concentration in the euphotic layer. At the same time, the AC brings CHLa into the  
791 euphotic layer by meridional advection, as the EUC has relatively high CHLa concentrations (Radenac  
792 et al., 2020). This low nitrate / high CHLa signature of the AC can be seen in the first hundred metres  
793 and in particular at the base of the euphotic layer along the Gabon-Congo coast (Fig.A1c), where the  
794 AC flows (Kopte et al, 2017). Further analyses show that the coastal CHLa maximum occurs from  
795 May to September with a peak in August, which is consistent with the seasonal cycle of the CHLa  
796 concentration in the EUC (Radenac et al, 2020; Brandt et al, 2023). The simultaneous variation in  
797 current and gradient appears to be the main factor contributing to variations in the meridional  
798 advection and nitrate removal, mainly between July and October. Over the same period, we observe a  
799 sign change of the meridional nitrate gradient (Fig.14b), which is generally positive (indicating that  
800 under the mixed layer, waters to the south of the coastal box (0°N–6°S, 1° width from the coast; see  
801 Fig. 1b) are less nitrate-rich than waters to the north) under the mixed layer from January to June.



802

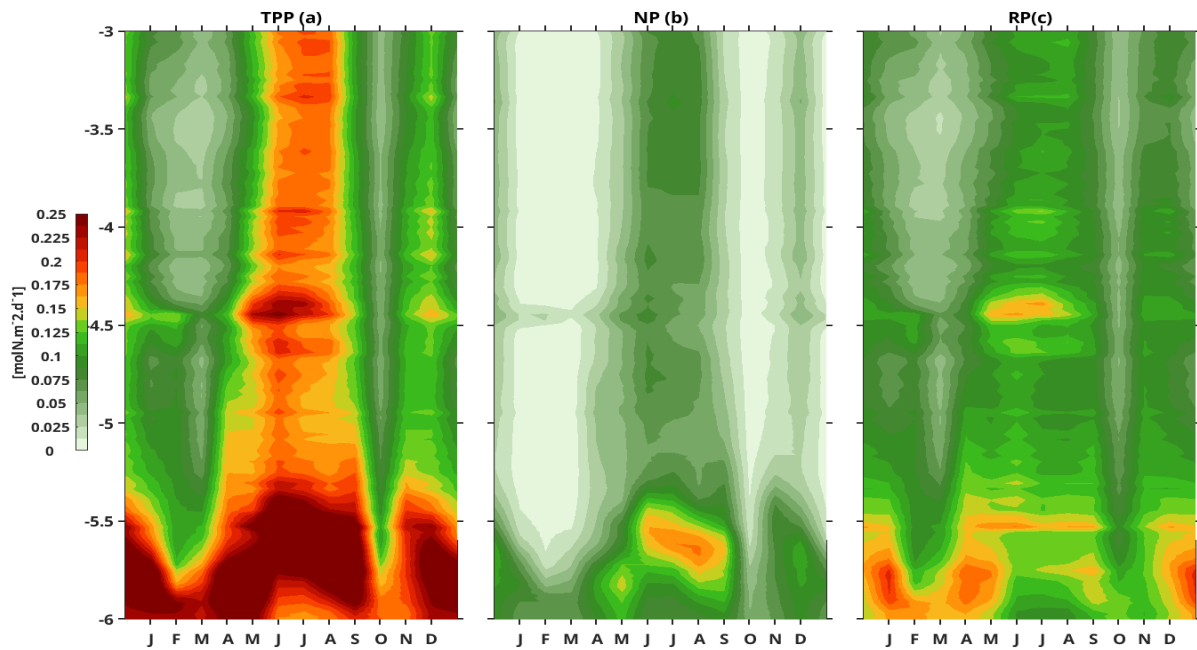
803 **Figure 16:** Regional distribution of mean annual nitrate and CHLa concentration (a, b respectively) averaged on  
 804 the 0-100 m layer along the Gabon-Congo upwelling area, black line represents different boundaries of our  
 805 Coastal box with a width of 1° of longitude relative to the coast.

806 This observation suggests that for the period from September to October, waters in the southern part of  
 807 the box are now richer in nitrate than waters in the northern part of the box under the mixed layer.  
 808 Beyond horizontal transport, this frontogenesis is also driven by the meridional gradient of vertical  
 809 motion ( $\partial w/\partial y$ ). A stronger upward vertical velocity in the southern section (near 6°S) compared to the  
 810 north leads to a higher vertical nitrate supply in the south, establishing the negative meridional nitrate  
 811 gradient observed in Fig. 14b. This highlights the important role of vertical processes in the regional  
 812 enrichment, as also emphasized by Nubi et al. (2016) for the equatorial band. This also reflects the  
 813 passage of low-nitrate waters from the EUC via the Angola Current to the Gabon-Congo coast.  
 814 However, we find that zonal advection brings nitrate in the euphotic layer and its decomposition has  
 815 shown that its variation is mostly influenced by zonal nitrate gradient variation, with a secondary  
 816 contribution of zonal current variation. This zonal current variation is seen to remove nitrate in the  
 817 euphotic layer during February-March and July-October. We can also see that in these periods the  
 818 zonal current flows toward the coast, which suggests that it brings low nitrate water from offshore  
 819 toward the coast. This seasonally eastward current is consistent with the seasonal cycle of SEUC  
 820 (Siegfried et al., 2019; Assene et al., 2022). Besides this, we can also see that there is a sign change of  
 821 the zonal nitrate gradient (Fig.13b) which occurs simultaneously with the sign change of the  
 822 meridional nitrate gradient (Fig.14b) suggesting that this inversion in zonal nitrate gradient is due to  
 823 Angola Current water at the coast. In fact, this later result highlights that the Angolan Current waters  
 824 flowing along the coast are less rich in nitrate than the water brought from offshore toward the coast by  
 825 the SEUC. As nitrate concentration in the coast is lower, SEUC waters act to increase nitrate  
 826 concentration in our coastal box, through zonal advection in the euphotic layer from April to  
 827 December. The CHLa budget analysis (Appendix A, Fig. A1) shows that the SEUC brings through  
 828 zonal advection low CHLa water at the coast thereby reducing the nitrate input during the

829 downwelling period. In the nitrate budget we saw that the main driver of nitrate input was vertical  
830 advection associated with CTWs. Körner et al. (2024) have shown, using satellite and mooring data,  
831 that CTWs detected in the SLA are of the low vertical mode, while the movement of the isopycnals is  
832 rather consistent with the vertical velocity structure of higher modes. This explains why isopycnals  
833 reach their seasonal minimum/maximum depth (in phase with the nitracline) after the minimum in  
834 SLA (Körner et al, 2024). The spatial distribution of mean annual nitrate and CHLa concentrations  
835 (Fig. 16a, b) provides clear evidence of the influence of the Angola Current (AC) on the coastal  
836 biogeochemistry of the Gabon-Congo system. Physically, the AC is a southward-flowing coastal  
837 current that advects warm, equatorial-origin waters along the shelf. Biogeochemically, our model  
838 results (Fig. 16a) show that while the broader coastal box is enriched in nutrients due to upwelling and  
839 riverine inputs, there is a distinct relative decrease in nitrate concentrations strictly along the shoreline,  
840 particularly south of 5°S. In this narrow coastal band,  $\text{NO}_3$  values are lower than those found in the core  
841 of the upwelling plume located slightly further offshore. Conversely, the chlorophyll-a map (Fig. 16b)  
842 reveals a robust coastal belt with maximum concentrations exceeding  $4.5 \text{ mg}\cdot\text{m}^{-3}$  right at the coast.  
843 This low-nitrate / high-CHLa inverse relationship at the immediate coastline is consistent with the  
844 known characteristics of the Angola Current. Indeed, the AC transports mature waters originating from  
845 the Equatorial Undercurrent (EUC).

846 We assessed the variability of biological productivity using the PISCES component of our coupled  
847 model (Fig. 18). The results show a clear semi-annual cycle of Net Primary Production (NPP), New  
848 Production (NP), and Regenerated Production (RP), which is consistent with the seasonal cycle of  
849 nitrate and CHLa concentrations observed in the region (Körner et al., 2024). The highest values of  
850 NPP (Fig. 17a) are found near the Congo River mouth (between 5.5°S and 6°S), where average values  
851 exceed  $0.20 \text{ mol N}\cdot\text{m}^{-2}\cdot\text{d}^{-1}$ . During the main upwelling period (June–August), the NPP reaches its  
852 maximum, with local peaks near 6°S exceeding  $0.25 \text{ mol N}\cdot\text{m}^{-2}\cdot\text{d}^{-1}$ . This intensity is comparable to,  
853 though slightly lower than, the average primary production reported for the Benguela and Humboldt  
854 systems, which reach  $0.37$  and  $0.33 \text{ mol N}\cdot\text{m}^{-2}\cdot\text{d}^{-1}$  respectively (converted from Tilstone et al., 2009;  
855 Monteiro et al., 2010).

856 The secondary upwelling period in December also shows high productivity, with NPP values reaching  
857 approximately  $0.22 \text{ mol N}\cdot\text{m}^{-2}\cdot\text{d}^{-1}$  near the river mouth. In contrast, during the downwelling periods  
858 (notably in March and October), the system becomes less productive, with NPP dropping below  
859  $0.075 \text{ mol N}\cdot\text{m}^{-2}\cdot\text{d}^{-1}$  in most of the coastal box. The analysis of production components reveals that  
860 during the main upwelling season, the New Production (NP) (Fig. 17b) peaks at around  
861  $0.15 \text{ mol N}\cdot\text{m}^{-2}\cdot\text{d}^{-1}$ , representing about 50–60% of the NPP. In December, the NP contribution is  
862 lower, around  $0.10 \text{ mol N}\cdot\text{m}^{-2}\cdot\text{d}^{-1}$ . The Regenerated Production (RP) (Fig. 17c) remains a significant  
863 and stable driver of productivity throughout the year, particularly near the Congo mouth where it often  
864 exceeds  $0.125 \text{ mol N}\cdot\text{m}^{-2}\cdot\text{d}^{-1}$ , highlighting the importance of nutrient recycling in this river-influenced  
865 system.



867

868 **Figure 17:** Latitude-Time Hovmöller diagram of biological productivity: Net Primary Production (a), New  
 869 Production (b) and regenerated Production (c) in the coastal box (6°S-3°S, 1° wide along the coastline). The  
 870 units are milli mol per cubic meter per day.

871 High values of Net Primary Production (NPP) are also observed around 4.47°S, near the mouth of the  
 872 Kouilou River, following the characteristic semi-annual cycle of the region. A detailed comparison of  
 873 the production components (Fig. 17b, c) reveals that Regenerated Production (RP), fueled by the  
 874 recycling of nutrients within the euphotic layer, is generally higher than New Production (NP). These  
 875 two parameters remain consistent with the seasonal cycle of nitrate concentrations described  
 876 previously.

877 The seasonal cycle of NPP in the Gabon-Congo system differs from those of the Benguela upwellings  
 878 (including the Namibian area), which are primarily wind-forced systems (Gutknecht et al., 2013). A  
 879 key distinction lies in the efficiency of nitrate utilization: in our study area, the contribution of New  
 880 Production to the total NPP is notably high. For instance, while the *f-ratio* (NP/NPP) in the Benguela  
 881 system typically ranges between 0.2 and 0.4 (Monteiro et al., 2010), it reaches approximately 0.6 in  
 882 the Gabon-Congo coastal box, indicating that more than half of the primary production is sustained by  
 883 the upward supply of new nitrates.

884 Finally, we demonstrate that the conclusions regarding the nitrate budget are highly sensitive to the  
 885 definition of the Mixed Layer Depth (MLD). In this study, we adopted a 3 m reference depth for the  
 886 MLD calculation, following the criterion proposed by Aroucha et al. (2025). This shallower definition  
 887 is more appropriate for the Gabon-Congo system, as it accurately captures the intense surface  
 888 stratification induced by the river's freshwater plume. With this refined MLD criterion, our results  
 889 show a significant shift in the balance of vertical processes: vertical diffusion (mixing) now emerges as  
 890 the dominant mechanism supplying nitrate to the mixed layer, outweighing the contribution of vertical

891 advection. This finding aligns with recent observations in the Angolan upwelling (Brandt et al., 2023;  
892 Körner et al., 2023, 2024) and the Gabon-Congo plume region (Scannell and McPhaden, 2018;  
893 Ngakala et al., 2025), which highlight turbulent mixing—often fueled by internal tides and shear—as a  
894 major driver of vertical nutrient and heat fluxes. This shift emphasizes the critical role of the 'Barrier  
895 Layer' and the strong surface halocline in trapping nutrients and modulating their upward transfer  
896 through small-scale mixing processes rather than mean vertical motion.

## 897 **5 Conclusion**

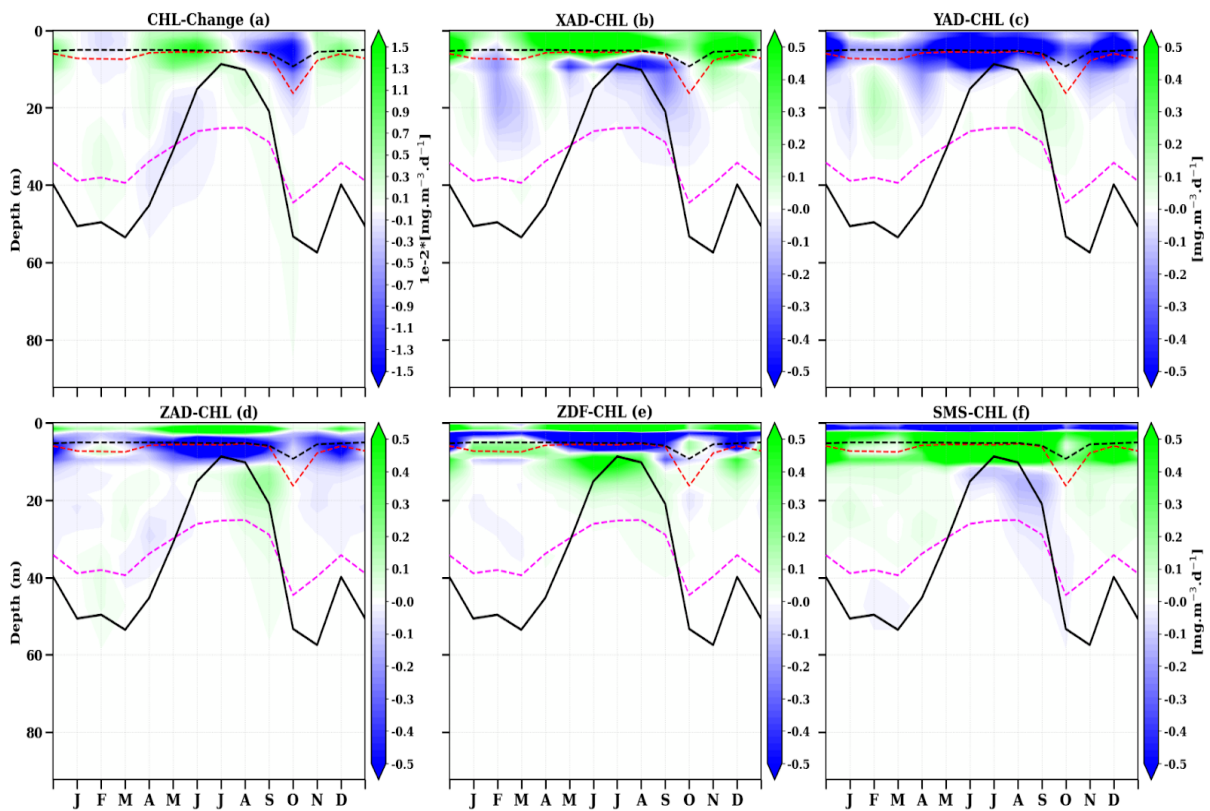
898 Throughout this work we have described and analysed the seasonal cycles in nitrate and CHLa  
899 concentrations, as well as the physical and biological processes that modulate nitrate supply and  
900 biological productivity in the mixed layer and in the euphotic layer in the Gabon-Congo upwelling  
901 system. We began by validating a regional high-resolution ( $1/36^\circ$ ) simulation of the coupled  
902 physical-biogeochemical model NEMO-PISCES in this area for the studied year 2011. Surface and  
903 subsurface validation of the simulation using observations (satellite, in situ, climatology) shows that  
904 the model reasonably reproduces the main physical and biogeochemical characteristics of the study  
905 area. Subsequently, the seasonal cycle of nitrate shows that there are two periods of upwelling and two  
906 periods of downwelling (Fig. 4e,f and Fig. 11a). These upwelling and downwelling are associated with  
907 remote forcing : Kelvin waves that propagate along the equator and the coastal waveguide force the  
908 vertical migrations of the thermocline, which is also a proxy for the nitracline. The seasonal cycle of  
909 CHLa is explained by that of nitrate. The assessment of the nitrate balance in the mixed layer shows  
910 that the main nitrate is mainly supplied in the mixed layer by vertical diffusion (Fig. 10f), vertical  
911 advection (Fig. 10d) and zonal advection (Fig. 10c), which is mainly modulated by nitrate inputs from  
912 the Congo River at  $6^\circ\text{S}$ . The vertical advection induced by CTWs and vertical diffusion play also a  
913 role in the nitrate supply, while nitrate losses are linked to meridional advection and the biological  
914 activity (photosynthesis). In the lower part of the euphotic layer, on the other hand, nitrate is supplied  
915 by zonal advection and vertical advection. Vertical diffusion contributes to nitrate losses, except in  
916 downwelling periods where it represents one of the main drivers of nitrate supply. We have also seen  
917 that meridional advection via the Angola Current, which transports the low-nitrate warm waters of the  
918 Equatorial undercurrent, is the main driver of nitrate loss below the mixed layer throughout the year.  
919 We find that vertical advection is controlled by the vertical nitrate gradient and nitrate input (Fig. 15),  
920 rather than vertical velocity, when it brings nitrate into the mixed layer during the main upwelling  
921 period. However, in the secondary upwelling in December, vertical advection also brings nitrate, but is  
922 then mostly controlled by vertical velocity.

923 In future works, the interannual variability will be studied, specifically in association with the  
924 interannual variability of the Congo River discharges (Scannell and McPhaden (2018), Körner et al.,  
925 2023, 2024; Brandt et al., 2023) and of the CTWs forced by the Equatorial Kelvin waves (e.g.  
926 Bachèlery et al., 2015, 2016). Understanding the seasonal and interannual variability of productivity is

927 of primary interest to ensure the sustainability of ecosystems and fisheries in the Gabon-Congo  
 928 upwelling system.

### 929 Appendix A : Euphotic Layer CHLa Budget Analysis

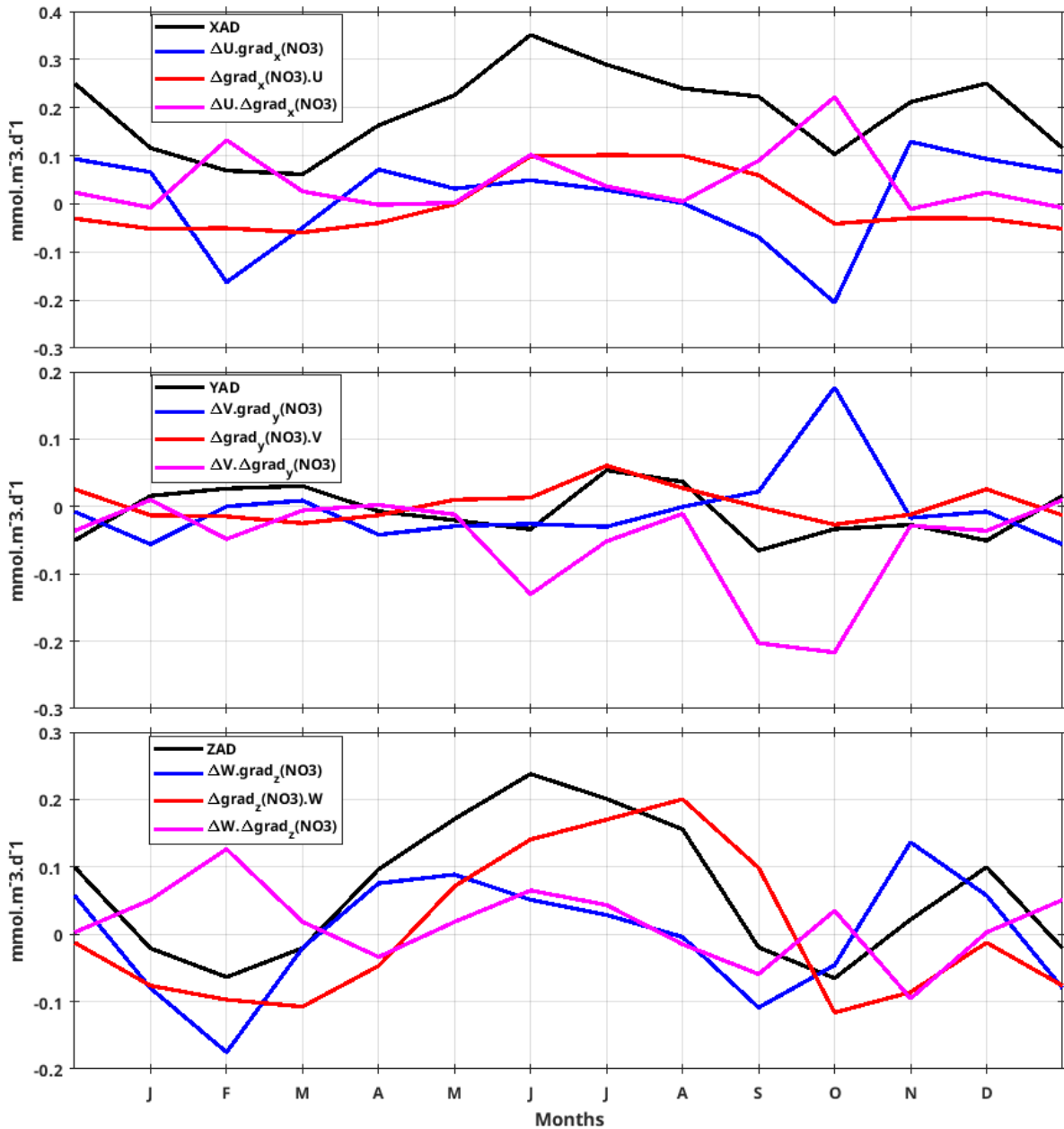
930 In the lower part of the euphotic zone, the CHLa budget (Fig. A1) is primarily governed by the  
 931 interaction between coastal and offshore water masses. During the downwelling period, the zonal  
 932 advection term (XAD\_CHL) shows a net loss of CHLa near the base of the euphotic layer. This is  
 933 explained by the passage of the South Equatorial Undercurrent (SEUC). As described by Nubi et al.  
 934 (2016), undercurrent waters (EUC/SEUC) are relatively nitrate-poor and carry less CHLa than the  
 935 highly productive coastal waters. The eastward transport of these offshore waters towards the  
 936 Gabon-Congo coast leads to a dilution of the local CHLa concentration, a process captured by the  
 937 negative values in the zonal advection budget.



938 **Figure A1:** Depth-time Hovmöller diagram of the seasonal chlorophyll-a budget along the Gabon-Congo coast  
 939 (6°S–0°N, 1° coastal strip) for: (a) total rate of change (CHL-change), (b) zonal advection (XAD-CHL), (c)  
 940 meridional advection (YAD-CHL), (d) vertical advection (ZAD-CHL), (e) vertical diffusion (ZDF-CHL), and (f)  
 941 biological source-minus-sink term (SMS-CHL). Units for all panels are  $\text{mg m}^{-3} \text{d}^{-1}$ . The black solid line  
 942 represents the thermocline (20°C isotherm), while dashed magenta, red and black lines indicate the euphotic,  
 943 isothermal and mixed layer depths, respectively.

### 945 Appendix B : Euphotic Layer Nitrate Advections Components Analysis

946 To further investigate this relationship, the individual contributions of seasonal current and  
 947 gradient variations are shown in **Appendix B (Fig. B1)**. This decomposition confirms that the  
 948 mean flow acting on seasonal gradient anomalies is the dominant driver of advection variability.



949

950 **Figure B1:** Seasonal variation of advection components averaged in the euphotic layer, black line represent  
 951 zonal, meridional and vertical advection in (a), (b) and (c) respectively. The red line in both three figures  
 952 represents gradient variation, blue line is current variation and magenta line represents the simultaneous  
 953 variation of gradient and current.

954 **Code and data availability.** Publicly available datasets were used for this study. Chlorophyll data  
 955 (1998–2020) are from the Copernicus-GlobColour dataset (<https://doi.org/10.48670/moi-00281>,  
 956 Copernicus, 2023a). The sea level anomaly data (1998–2020) were accessed via the Copernicus Server  
 957 (<https://doi.org/10.48670/moi-00148>, Copernicus, 2023b). The MUR SST product created by the JPL

958 MUR MEaSURES program as part of the GHRSSST (Group for High-Resolution Sea Surface  
959 Temperature) project is obtained from <https://podaac.jpl.nasa.gov/dataset/MUR-JPL-L4-GLOB-v4.1>  
960 (Chin et al., 2017) and ASCAT wind data <https://podaac.jpl.nasa.gov/dataset/ASCATB-L2-25km>. The  
961 nutrient fields were assessed using the CSIRO Atlas of Regional Seas climatology (Dunn and  
962 Ridgway, 2002) ,  
963 <https://portal.aodn.org.au/search?uuid=d9302a48-57b1-41c2-a0dc-78bd00dd5e4b>. Near surface  
964 currents from the Ocean Surface Current Analysis Real-time (OSCAR, Johnson et al. 2007),  
965 [https://podaac.jpl.nasa.gov/dataset/OSCAR\\_L4\\_OC\\_INTERIM\\_V2.0](https://podaac.jpl.nasa.gov/dataset/OSCAR_L4_OC_INTERIM_V2.0). Model outputs are available  
966 from the authors, especially GA, ID, GM, and JJ.

967

968 **Author contributions.** LJME outlined and wrote the paper. LJME and RDG produced the figures.  
969 GM has run the NEMO-PISCES model. GA, ID, CYD the co-authors contributed to define  
970 methodology and reviewed the paper.

971 **Conflict of Interest.** The authors declare that they have no conflict of interest.

972 **Acknowledgments.** Research is sponsored by the CNES SWOT-ETAO project (Surface Water and  
973 Ocean Topography, Study of Ocean Topography and Altimetry by the National Centre for Space  
974 Studies France). GENCI GEN7298 project ( National High-Performance Computing Equipment) for  
975 computing hours for simulations.

976 Thanks go to ([https://podaac.jpl.nasa.gov/dataset/OSCAR\\_L4\\_OC\\_INTERIM\\_V2.0](https://podaac.jpl.nasa.gov/dataset/OSCAR_L4_OC_INTERIM_V2.0)) to provide  
977 OSCAR current data.

978 Also thanks to <https://podaac.jpl.nasa.gov/dataset/MUR-JPL-L4-GLOB-v4.1> for providing MUR SST  
979 data.

980 **Financial Support.** This project is funded by IRD-ARTS (Research Grant for a Thesis in the South  
981 provided by Institute of Research for Development France) for my Phd scholarship.

## 982 **References**

983 Assene, F., Morel, Y., Delpech, A., Aguedjou, M., Jouanno, J., Cravatte, S., Marin, F., Ménesguen, C.,  
984 Chaigneau, A., Dadou, I., Alory, G., Holmes, R., Bourlès, B., and Koch-larrouy, A.: From Mixing to  
985 the Large Scale Circulation: How the Inverse Cascade Is Involved in the Formation of the Subsurface  
986 Currents in the Gulf of Guinea, *Fluids*, 5, 147, <https://doi.org/10.3390/fluids5030147>, 2020.

987 Aumont, O. and Bopp, L.: Globalizing results from ocean insitu iron fertilization experiments, *Global  
988 Biogeochem. Cy.*, 20, GB2017, <https://doi.org/10.1029/2005GB002591>, 2006.

989 Aumont, O., Belviso, S., and Monfray, P.: Dimethylsulfide (DMS) cycle with a 3-D  
990 ocean-biogeochemical model, *Oceanogr. Lit. Rev.*, 11, 1637, <https://doi.org/10.1029/98GB02757>,  
991 1998.

- 992 Aumont, O., Ethé, C., Tagliabue, A., Bopp, L., and Gehlen, M.: PISCES-v2: an ocean biogeochemical  
993 model for carbon and ecosystem studies, *Geosci. Model Dev.*, 8, 2465–2513,  
994 <https://doi.org/10.5194/gmd-8-2465-2015>, 2015.
- 995 Awo, F. M., Alory, G., Da-Allada, C. Y., Delcroix, T., Jouanno, J., Kestenare, E., and Baloïtcha, E.: On  
996 the seasonal and interannual variability of the sea surface salinity in the Gulf of Guinea, *Clim.*  
997 *Dynam.*, 60, 2121–2140, <https://doi.org/10.1007/s00382-022-06443-4>, 2023.
- 998 Awo, F. M., Rouault, M., Ostrowski, M., Tomety, F. S., Da-Allada, C. Y., and Jouanno, J.: Seasonal  
999 cycle of sea surface salinity in the Angola Upwelling System, *J. Geophys. Res. Oceans*, 127,  
1000 e2022JC018518, <https://doi.org/10.1029/2022JC018518>, 2022.
- 1001 Bachèlery, M. L.: Variabilité côtière physique et biogéochimique en Atlantique Sud-Est: rôle du  
1002 forçage atmosphérique local versus téléconnexion océanique, PhD thesis, University of Paul Sabatier,  
1003 Toulouse, France, 215 pp., 2016.
- 1004 Bachèlery, M.-L., Illig, S., and Dadou, I.: Interannual variability in the South-East Atlantic Ocean,  
1005 focusing on the Benguela Upwelling System: Remote versus local forcing, *J. Geophys. Res. Oceans*,  
1006 121, 284–310, <https://doi.org/10.1002/2015JC011168>, 2015.
- 1007 Bourlès, B., Molinari, R. L., Johns, W. E., Gouriou, Y., and Carder, K. L.: The South Equatorial  
1008 Undercurrent in the Atlantic Ocean, *Geophys. Res. Lett.*, 31, L14301,  
1009 <https://doi.org/10.1029/2004GL020020>, 2004.
- 1010 Brandt, P., Alory, G., Awo, F. M., Dengler, M., Djakouré, S., Imbol Koungue, R. A., Jouanno, J.,  
1011 Körner, M., Roch, M., and Rouault, M.: Physical processes and biological productivity in the  
1012 upwelling regions of the tropical Atlantic, *Ocean Sci.*, 19, 581–601,  
1013 <https://doi.org/10.5194/os-19-581-2023>, 2023.
- 1014 Cabos, W., Sein, D. V., Pinto, J. G., Koseki, S., Álvarez-García, F. J., and Durán-Quesada, A. M.: The  
1015 coastal upwelling system of the southeast Atlantic as simulated by a high-resolution coupled model,  
1016 *Clim. Dynam.*, 49, 1809–1828, <https://doi.org/10.1007/s00382-016-3319-9>, 2017.
- 1017 Caniaux, G., Giordani, H., Redelsperger, J. L., Guichard, F., Key, E., and Wade, M.: Coupling between  
1018 the Atlantic cold tongue and the West African monsoon in boreal spring and summer, *J. Geophys. Res.*  
1019 *Oceans*, 116, C04003, <https://doi.org/10.1029/2010jc006570>, 2011.
- 1020 Carr, M.-E.: Estimation of potential productivity in Eastern Boundary Currents using remote sensing,  
1021 *Deep-Sea Res. Pt. II*, 49, 59–80, [https://doi.org/10.1016/S0967-0645\(01\)00094-7](https://doi.org/10.1016/S0967-0645(01)00094-7), 2002.
- 1022 Chavez, F. P. and Messié, M.: A comparison of eastern boundary upwelling ecosystems, *Prog.*  
1023 *Oceanogr.*, 83, 80–96, <https://doi.org/10.1016/j.pocean.2009.07.032>, 2009.
- 1024 Chin, T. M., Vazquez-Cuervo, J., and Armstrong, E.: A multi-scale high-resolution analysis of global  
1025 sea surface temperature, *Remote Sens. Environ.*, 200, 154–169,  
1026 <https://doi.org/10.1016/j.rse.2017.07.029>, 2017.
- 1027 de Boyer Montégut, C., Madec, G., Fischer, A. S., Lazar, A., and Iudicone, D.: Mixed layer depth over  
1028 the global ocean: An examination of profile data and a profile-based climatology, *J. Geophys. Res.*  
1029 *Oceans*, 109, C12003, <https://doi.org/10.1029/2004JC002378>, 2004.

1030 Bonhoure, D., Rowe, E., Mariano, A. J., and Ryan, E. H.: The South Equatorial Sys Current, Ocean  
1031 Surface Currents, available at: <https://oceancurrents.rsmas.miami.edu/atlantic/south-equatorial.html>  
1032 (last access: 18 February 2026), 2004.

1033 Dossa, A., Da-Allada, C., Herbert, G., and Bourlès, B.: Seasonal cycle of the salinity barrier layer  
1034 revealed in the northeastern Gulf of Guinea, *Afr. J. Mar. Sci.*, 41, 163–175,  
1035 <https://doi.org/10.2989/1814232X.2019.1616612>, 2019.

1036 Ducet, N., Le Traon, P.-Y., and Reverdun, G.: Global high-resolution mapping of ocean circulation  
1037 from TOPEX/Poseidon and ERS-1 and -2, *J. Geophys. Res. Oceans*, 105, 19477–19498,  
1038 <https://doi.org/10.1029/2000jc900063>, 2000.

1039 Dunn, J. R. and Ridgway, K. R.: Mapping ocean properties in regions of complex topography,  
1040 *Deep-Sea Res. Pt. I*, 49, 591–604, [https://doi.org/10.1016/S0967-0637\(01\)00069-3](https://doi.org/10.1016/S0967-0637(01)00069-3), 2002.

1041 Estival, R., Quiniou, V., and Messenger, C.: Real-time network of weather and ocean stations:  
1042 public-private partnership on in-situ measurements in the Gulf of Guinea, *Sea Technol.*, 54, 34–38,  
1043 2013.

1044 FAO: Fishery and Aquaculture Country Profiles, Angola, Country Profile Fact Sheets, Fisheries and  
1045 Aquaculture Division [online], available at: <https://www.fao.org/fishery/en/facp/ago?lang=en> (last  
1046 access: 11 April 2023), 2022.

1047 Fréon, P., Barange, M., and Arístegui, J.: Eastern boundary upwelling ecosystems: integrative and  
1048 comparative approaches, *Prog. Oceanogr.*, 83, 1–14, <https://doi.org/10.1016/j.pocean.2009.07.014>,  
1049 2009.

1050 Gutknecht, E., Dadou, I., Marchesiello, P., Cambon, G., Le Vu, B., Sudre, J., Garçon, V., Machu, E.,  
1051 Rixen, T., Kock, A., Flohr, A., Paulmier, A., and Lavik, G.: Nitrogen transfers off Walvis Bay: a 3-D  
1052 coupled physical/biogeochemical modeling approach in the Namibian upwelling system,  
1053 *Biogeosciences*, 10, 4117–4135, <https://doi.org/10.5194/bg-10-4117-2013>, 2013.

1054 Hardman-Mountford, N. J. and McGlade, J. S.: Retrieval of phytoplankton biomass from ocean colour  
1055 in the Benguela ecosystem, *Remote Sens. Environ.*, 79, 11–23,  
1056 [https://doi.org/10.1016/S0034-4257\(01\)00236-0](https://doi.org/10.1016/S0034-4257(01)00236-0), 2002.

1057 Hopkins, J., Lucas, M., Dufau, C., Sutton, M., Stum, J., Lauret, O., and Channelliere, C.: Detection  
1058 and variability of the Congo River plume from satellite derived sea surface temperature, salinity, ocean  
1059 colour and sea level, *Remote Sens. Environ.*, 139, 365–385, <https://doi.org/10.1016/j.rse.2013.08.015>,  
1060 2013.

1061 Hutchings, L., van der Lingen, C. D., Shannon, L. J., Crawford, R. J. M., Verheye, H. M. S.,  
1062 Bartholomae, C. H., van der Plas, A. K., Louw, D., Kreiner, A., Ostrowski, M., Fidel, Q., Barlow, R.  
1063 G., Lamont, T., Coetzee, J., Shillington, F., Veitch, J., Currie, J. C., and Monteiro, P. M. S.: The  
1064 Benguela Current: An ecosystem of four components, *Prog. Oceanogr.*, 83, 15–32,  
1065 <https://doi.org/10.1016/j.pocean.2009.07.046>, 2009.

1066 Johns, W. E., Brandt, P., Lumpkin, R., Fischer, J., Hormann, V., Pirani, A., Schmid, C., and Bourlès,  
1067 B.: Variation of upper ocean seasonal and interannual velocity structure in the eastern equatorial  
1068 Atlantic, *J. Phys. Oceanogr.*, 44, 1201–1212, <https://doi.org/10.1175/JPO-D-13-0132.1>, 2014.

1069 Johnson, E. S., Bonjean, F., Lagerloef, G. S., Gunn, J. T., and Mitchum, G. T.: Validation and error  
1070 analysis of OSCAR sea surface currents, *J. Atmos. Ocean. Tech.*, 24, 688–701,  
1071 <https://doi.org/10.1175/JTECH1971.1>, 2007.

1072 Jouanno, J.: Influence de la dynamique de l'Atlantique équatorial sur la variabilité de la langue froide,  
1073 PhD thesis, Université de Toulouse III, France, 2010.

1074 Kobayashi, S., Ota, Y., Harada, Y., Ebita, A., Moriya, M., Onoda, H., Onogi, K., Kamiguchi, H.,  
1075 Kobayashi, C., Endo, H., Miyaoka, K., and Takahashi, K.: The JRA-55 Reanalysis: General  
1076 specifications and basic characteristics, *J. Meteorol. Soc. Jpn.*, 93, 5–48,  
1077 <https://doi.org/10.2151/jmsj.2015-001>, 2015.

1078 Kopte, R.: The Angola Current in a Tropical Seasonal Upwelling System: Seasonal Variability in  
1079 Response to Remote Equatorial and Local Forcing, PhD thesis, Christian-Albrechts Universität Kiel,  
1080 Germany, 2017.

1081 Körner, M., Brandt, P., and Dengler, M.: Seasonal cycle of sea surface temperature in the tropical  
1082 Angolan Upwelling System, *Ocean Sci.*, 19, 121–139, <https://doi.org/10.5194/os-19-121-2023>, 2023.

1083 Körner, M., Brandt, P., Illig, S., Dengler, M., Subramaniam, A., Bachèlery, M. L., and Krahnemann, G.:  
1084 Coastal trapped waves and tidal mixing control primary production in the tropical Angolan upwelling  
1085 system, *Sci. Adv.*, 10, adj6686, <https://doi.org/10.1126/sciadv.adj6686>, 2024.

1086 Locarnini, M. M., Mishonov, A. V., Baranova, O. K., Boyer, T. P., Zweng, M. M., Garcia, H. E.,  
1087 Mishonov, A., and Smolyar, I.: World ocean atlas 2018, volume 1: Temperature, NOAA Atlas  
1088 NESDIS, 81, 2018.

1089 Koseki, S., Cabos, W., Sein, D. V., and Mohino, E.: The role of the Gulf of Guinea upwelling in the  
1090 atmospheric circulation of the tropical Atlantic in a high-resolution coupled model, *Clim. Dynam.*, 51,  
1091 1017–1035, <https://doi.org/10.1007/s00382-017-3896-2>, 2018.

1092 Koubanova, M., Koseki, S., and Keenlyside, N. S.: Seasonal variability of the Atlantic cold tongue and  
1093 its relationship with the Angola-Benguela upwelling system, *Clim. Dynam.*, 51, 2975–2993,  
1094 <https://doi.org/10.1007/s00382-018-4197-0>, 2018.

1095 Loukos, H. and Mémerly, L.: Simulation of the nitrate seasonal cycle in the equatorial Atlantic ocean  
1096 during 1983 and 1984, *J. Geophys. Res. Oceans*, 104, 15549–15573,  
1097 <https://doi.org/10.1029/1999JC900084>, 1999.

1098 Madec, G. and the NEMO System Team: NEMO Ocean Engine Reference Manual, Zenodo [code],  
1099 <https://doi.org/10.5281/zenodo.1464816>, 2024.

1100 Messié, M. and Chavez, F. P.: Seasonal regulation of primary production in eastern boundary  
1101 upwelling systems, *Prog. Oceanogr.*, 134, 1–18, <https://doi.org/10.1016/j.pocean.2014.10.011>, 2015.

1102 Monteiro, P., Dewitte, B., Scranton, M., Paulmier, A., and Van der Plas, A.: The role of open ocean  
1103 boundary forcing on seasonal to decadal-scale variability and long-term change of natural shelf  
1104 hypoxia, *Environ. Res. Lett.*, 6, 024002, <https://doi.org/10.1088/1748-9326/6/2/024002>, 2011.

- 1105 Ngakala, R. D., Alory, G., Da-Allada, C. Y., Dadou, I., Cardot, C., Morvan, G., and Baloïtcha, E.:  
1106 Seasonal mixed layer temperature in the Congolese upwelling system, *J. Geophys. Res. Oceans*, 130,  
1107 e2023JC020528, <https://doi.org/10.1029/2023JC020528>, 2025.
- 1108 Nieto, K. and Mélin, F.: Variability of chlorophyll-a concentration in the Gulf of Guinea and its  
1109 relation to physical oceanographic variables, *Prog. Oceanogr.*, 151, 97–115,  
1110 <https://doi.org/10.1016/j.pocean.2016.12.001>, 2017.
- 1111 Nubi, O., Bourles, B., and Edokpayi, C.: On the Nutrient distribution and phytoplankton biomass in  
1112 the Gulf of Guinea equatorial band as inferred from In-situ measurements, *J. Oceanogr. Mar. Sci.*, 7,  
1113 1–11, <https://doi.org/10.5897/JOMS2015.0125>, 2016.
- 1114 Ostrowski, M., da Silva, J. C. B., and Bazik-Sangolay, B.: The response of sound scatterers to El Niño-  
1115 and La Niña-like oceanographic regimes in the southeastern Atlantic, *ICES J. Mar. Sci.*, 66,  
1116 1063–1072, <https://doi.org/10.1093/icesjms/fsp102>, 2009.
- 1117 Radenac, M.-H., Jouanno, J., Tchamabi, C. C., Awo, M., Bourlès, B., Arnault, S., and Aumont, O.:  
1118 Physical drivers of the nitrate seasonal variability in the Atlantic cold tongue, *Biogeosciences*, 17,  
1119 529–545, <https://doi.org/10.5194/bg-17-529-2020>, 2020.
- 1120 Resplandy, L., Hogikyan, A., Müller, J. D., Najjar, R. G., Bange, H. W., Bianchi, D., and Regnier, P.: A  
1121 synthesis of global coastal ocean greenhouse gas fluxes, *Global Biogeochem. Cy.*, 38,  
1122 e2023GB007803, <https://doi.org/10.1029/2023GB007803>, 2024.
- 1123 Ridgway, K. R., Dunn, J. R., and Wilkin, J. L.: Ocean interpolation by four-dimensional least  
1124 squares—Application to the waters around Australia, *J. Atmos. Ocean. Tech.*, 19, 1357–1375,  
1125 [https://doi.org/10.1175/1520-0426\(2002\)019<1357:OIBFDL>2.0.CO;2](https://doi.org/10.1175/1520-0426(2002)019<1357:OIBFDL>2.0.CO;2), 2002.
- 1126 Rouault, M.: Bi-annual intrusion of tropical water in the northern Benguela upwelling, *Geophys. Res.*  
1127 *Lett.*, 39, L12606, <https://doi.org/10.1029/2012gl052099>, 2012.
- 1128 Scannell, H. A. and McPhaden, M. J.: Seasonal mixed layer temperature balance in the southeastern  
1129 tropical Atlantic, *J. Geophys. Res. Oceans*, 123, 5557–5570, <https://doi.org/10.1029/2018JC014099>,  
1130 2018.
- 1131 Schott, F. A., Fischer, J., and Stramma, L.: Transports and pathways of the upper-layer circulation in  
1132 the western tropical Atlantic, *J. Phys. Oceanogr.*, 28, 1904–1928,  
1133 [https://doi.org/10.1175/1520-0485\(1998\)028<1904:TAPOTU>2.0.CO;2](https://doi.org/10.1175/1520-0485(1998)028<1904:TAPOTU>2.0.CO;2), 1998.
- 1134 Siegfried, L., Schmidt, M., Mohrholz, V., Pogrzeba, H., Nardini, P., Böttinger, M., and Scheuermann,  
1135 G.: The tropical-subtropical coupling in the Southeast Atlantic from the perspective of the northern  
1136 Benguela upwelling system, *PLOS ONE*, 14, e0210083, <https://doi.org/10.1371/journal.pone.0210083>,  
1137 2019.
- 1138 Sikhakolli, R., Sharma, R., Basu, S., Gohil, B. S., Sarkar, A., and Prasad, K. V. S. R.: Evaluation of  
1139 OSCAR ocean surface current product in the tropical Indian Ocean using in situ data, *J. Earth Syst.*  
1140 *Sci.*, 122, 187–199, <https://doi.org/10.1007/s12040-012-0258-0>, 2013.

- 1141 Sowman, M. and Cardoso, P.: Small-scale fisheries and food security strategies in countries in the  
1142 Benguela Current Large Marine Ecosystem (BCLME) region: Angola, Namibia and South Africa,  
1143 *Mar. Policy*, 34, 1163–1170, <https://doi.org/10.1016/j.marpol.2010.03.016>, 2010.
- 1144 Tchupalanga, P., Dengler, M., Brandt, P., Kopte, R., Macueria, M., Coelho, P., Ostrowski, M., and  
1145 Keenlyside, N. S.: Eastern Boundary Circulation and Hydrography Off Angola: Building Angolan  
1146 Oceanographic Capacities, *B. Am. Meteorol. Soc.*, 99, 1589–1605,  
1147 <https://doi.org/10.1175/Bams-D-17-0197.1>, 2018.
- 1148 Thiam, A., Alory, G., Jouanno, J., Da-Allada, C. Y., and Morvan, G.: Coastal upwelling in the  
1149 Northern Gulf of Guinea: Seasonal cycle and mesoscale interactions, *Ocean Model.*, 188, 102300,  
1150 <https://doi.org/10.1016/j.ocemod.2024.102300>, 2024.
- 1151 Tilstone, G., Smyth, T., Poulton, A., and Hutson, R.: Measured and remotely sensed estimates of  
1152 primary production in the Atlantic Ocean from 1998 to 2005, *Deep-Sea Res. Pt. II*, 56, 918–930,  
1153 <https://doi.org/10.1016/j.dsr2.2008.10.034>, 2009.
- 1154 Topé, G. D. A., Alory, G., Djakouré, S., Da-Allada, C. Y., Jouanno, J., and Morvan, G.: How does the  
1155 Niger River warm coastal waters in the Northern Gulf of Guinea?, *Front. Mar. Sci.*, 10, 1187202,  
1156 <https://doi.org/10.3389/fmars.2023.1187202>, 2023.
- 1157 Tuchen, F. P., Brandt, P., Lübbecke, J. F., and Hummels, R.: Transports and pathways of the tropical  
1158 AMOC return flow from Argo data and shipboard velocity measurements, *J. Geophys. Res. Oceans*,  
1159 127, e2021JC018115, <https://doi.org/10.1029/2021JC018115>, 2022.
- 1160 Voldoire, A., Belamari, S., and Lévy, M.: On the role of ocean-atmosphere interaction in the onset of  
1161 the Atlantic cold tongue, *Clim. Dynam.*, 53, 5437–5455, <https://doi.org/10.1007/s00382-019-04717-0>,  
1162 2019.
- 1163 Xu, Z., Li, M., Patricola, C. M., and Chang, P.: Oceanic origin of southeast tropical Atlantic biases,  
1164 *Clim. Dynam.*, 43, 2915–2930, <https://doi.org/10.1007/s00382-013-1901-y>, 2014.
- 1165 Zeng, Z., Brandt, P., Lamb, K. G., Greatbatch, R. J., Dengler, M., Claus, M., and Chen, X.:  
1166 Three-dimensional numerical simulations of internal tides in the Angolan upwelling region, *J.*  
1167 *Geophys. Res. Oceans*, 126, e2020JC016460, <https://doi.org/10.1029/2020JC016460>, 2021.
- 1168 Zuidema, P., Redemann, J., Haywood, J., Wood, R., Piketh, S., Hipondoka, M., and Formenti, P.:  
1169 Smoke and clouds above the southeast Atlantic: Upcoming field campaigns probe absorbing aerosol's  
1170 impact on climate, *B. Am. Meteorol. Soc.*, 97, 1131–1135,  
1171 <https://doi.org/10.1175/BAMS-D-15-00032.1>, 2016.
- 1172 Zweng, M. M., Seidov, D., Boyer, T. P., Locarnini, M., Garcia, H. E., Mishonov, A. V., and Smolyar,  
1173 I.: World ocean atlas 2018, volume 2: Salinity, NOAA Atlas NESDIS, 82, 2019.
- 1174